Naval Research Laboratory
Stennis Space Center, MS 39529-5004

Study of Environmental Influences on Phase Fluctuations and Their Effect on Synthetic Aperture Sonars (SAS)

Edward J. Yoerger

Naval Oceanographic Office
Stennis Space Center, MS 39529

Timothy H. Ruppel
J. Stephen Stanic
Acoustic Simulation, Measurements, and Tactics Branch
Acoustics Division

DTIC QUALITY INSPECTED 2

March 25, 1999

19990426 020

REPORT DOCUMENTATION PAGE

Public reporting burden for this collection of information is estimated to average 1 hour per response, including the time for reviewing instructions, searching existing data sources, gathering and maintaining the data needed, and completing and reviewing the collection of information. Send comments regarding this burden or any other aspect of this collection of information, including suggestions for reducing this burden, to Washington Headquarters Services, Directorate for information Operations and Reports, 1215 Jefferson Davis Highway, Suite 1204, Arlington, VA 22202-4302, and to the Office of Management and Budget, Paperwork Reduction Project (0704-0188), Washington, DC 20503.

1. AGENCY USE ONLY *(Leave blank)*	2. REPORT DATE March 25, 1999	3. REPORT TYPE AND DATES COVERED Final	

4. TITLE AND SUBTITLE Study of Environmental Influences on Phase Fluctuations and Their Effect on Synthetic Aperture Sonars (SAS)	5. FUNDING NUMBERS Job Order No. 71-6861-00 Program Element No. 0602435N
6. AUTHOR(S) Edward J. Yoerger*, Timothy H. Ruppel, and J. Stephen Stanic	Project No. Task No. UW-35-2-05 Accession No. DN 16-3758

7. PERFORMING ORGANIZATION NAME(S) AND ADDRESS(ES) Naval Research Laboratory Acoustics Division Stennis Space Center, MS 39529-5004	8. PERFORMING ORGANIZATION REPORT NUMBER NRL/MR/7184--99-8224
9. SPONSORING/MONITORING AGENCY NAME(S) AND ADDRESS(ES) Office of Naval Research 800 N. Quincy St. Arlington, VA 22217-5000	10. SPONSORING/MONITORING AGENCY REPORT NUMBER

11. SUPPLEMENTARY NOTES

*Naval Oceanographic Office, Stennis Space Center, MS 39529

12a. DISTRIBUTION/AVAILABILITY STATEMENT Approved for public release; distribution unlimited.	12b. DISTRIBUTION CODE

13. ABSTRACT *(Maximum 200 words)*

An acoustic propagation experiment designed to investigate how Synthetic Aperture Sonar (SAS) is affected by the underwater environment was conducted off the eastern U.S. coastline near Martha's Vineyard in August 1996. This report describes the effect of this shallow-water, underwater environment on the phase of propagating acoustic signals. This experiment made measurements of acoustic ping-to-ping phase fluctuations at a frequency of 20 kHz. These fluctuations were measured using a submersible tow body on which were mounted two acoustic arrays that received pulses transmitted once per second from sources that were mounted on two stationary, spatially separated towers. The phase fluctuations are calculated after correcting for any phase errors induced by the motion of the tow body. The results showed that the use of SAS techniques in this environment would be, at best, marginal at 20 kHz. The measured phase fluctuations led, in some cases, to theoretically calculated SAS beam patterns that were nearly omnidirectional.

14. SUBJECT TERMS MCM sonar system designs, high-frequency acoustics, spatial & temporal coherence	15. NUMBER OF PAGES 63
	16. PRICE CODE

17. SECURITY CLASSIFICATION OF REPORT Unclassified	18. SECURITY CLASSIFICATION OF THIS PAGE Unclassified	19. SECURITY CLASSIFICATION OF ABSTRACT Unclassified	20. LIMITATION OF ABSTRACT SAR

NSN 7540-01-280-5500

Study of Environmental Influences on Phase Fluctuations and Their Effect on Synthetic Aperture Sonars (SAS)

Edward J. Yoerger
Naval Oceanographic Office, Stennis Space Center, MS 39529

Timothy H. Ruppel, and Steve Stanic
Naval Research Laboratory, Stennis Space Center, MS 39529

Abstract

An acoustic propagation experiment designed to investigate how Synthetic Aperture Sonar (SAS) is affected by the underwater environment was conducted off the eastern U.S. coastline near Martha's Vineyard in August 1996. This report describes the effect of this shallow-water underwater environment on the phase of propagating acoustic signals. This experiment made measurements of acoustic ping-to-ping phase fluctuations at a frequency of 20 kHz. These fluctuations were measured using a submersible tow-body on which were mounted two acoustic arrays that received pulses transmitted once a second from sources that were mounted on two stationary, spatially separated towers. The phase fluctuations are calculated after correcting for any phase errors induced by the motion of the tow-body. The results showed that the use of SAS techniques in this environment would be, at best, marginal at 20 kHz. The measured phase fluctuations led, in some cases, to theoretically calculated SAS beam patterns that where nearly omnidirectional.

I.   Introduction

In Synthetic Aperture Sonar (SAS) operations, a moving receiver senses acoustic signals scattered from an ensonified target. Usually, the source of ensonification is the moving receiver platform itself and the target is repeatedly ensonified at constant time intervals. The spatial positions along the receiver flight path constitute the synthetic aperture array and precise measurements of these receiver positions are crucial for optimal SAS performance.

The flight path of the receiver, which forms the synthetic aperture, is usually not linear. For SAS, all that is required is that the receiving positions along the receiver track are well known. However, casting the SAS processing problem for a general flight path into that for a spatially linear flight path, as will be done herein, allows the use of widely known and well understood results from conventional beamforming using linear arrays.

When plane waves strike a linear array in a medium with a constant sound speed profile, the phase difference of the acoustic signal between elements of the array is also constant. The resulting beam pattern for such an unshaded, unsteered array is the absolute value of a sinc function $\left(\left|\sin\theta/\theta\right|\right)$. If the same array is placed in a medium with a sound speed profile that vaires in range and depth, the resulting beam pattern will deviate from the case of constant sound speed. The resulting SAS effect is a loss of array performance due to ping-to-ping fluctuations in the water column.

Near Martha's Vineyard, off the eastern U.S. coastline, an acoustic propagation experiment was performed in the summer of 1996 that investigated how the underwater environment could affect the performance of SAS. Sources mounted on spatially separated towers transmitted short (1 ms) acoustic pulses at 1-second intervals. The signals were received by two side-looking arrays mounted on a tow-body traversing an approximately linear underwater flight path. In this

paper, the phases of the received signals are analyzed in order to obtain the ping-to-ping phase fluctuations after compensation for tow-body motion. In addition to phase fluctuation results, this paper will present a comparison of the expected SAS beam pattern for an ideal case with no acoustic signal ping-to-ping fluctuations, and a case where the ping-to-ping fluctuations are based on measured values.

In Section II the experimental configurations and organization of the data collection effort are reported. Section III contains a description of the types of data collected, the instrumentation used, and the measurements made. The methodology used in the data analysis is discussed in Section IV. Section V describes theoretical calculations of the effect of phase variance and correlation length on the SAS beam power output. Section VI applies the results from of Section V to the data. Finally, Section VII gives the conclusions derived from the analysis.

II. Experiment Description

The experiment was performed during August 23-26, 1996, in approximately 50 m of water depth off the coast of Martha's Vineyard. The experimental configuration consisted of sources mounted on two stationary towers and a tow-body equipped with two side-looking receiver arrays. The source towers were 13 m high and were positioned approximately 800 m apart. The transducers mounted at the top of each tower simultaneously transmitted 1 ms, 20 kHz acoustic pings at 1-second intervals. The receiver arrays were towed from a ship at a depth of 20 m along paths parallel to an imaginary line connecting the towers at ranges of 50–400 m. The length of a path was limited to about 800 m. The experimental configuration is shown in Figure 1. The data collected for each range (track) constituted a single experimental run. Tow-body navigation, motion and attitude were also measured. The sea was calm throughout the experiment with swells less than 1 m and swell periods of 5 to 10 sec.
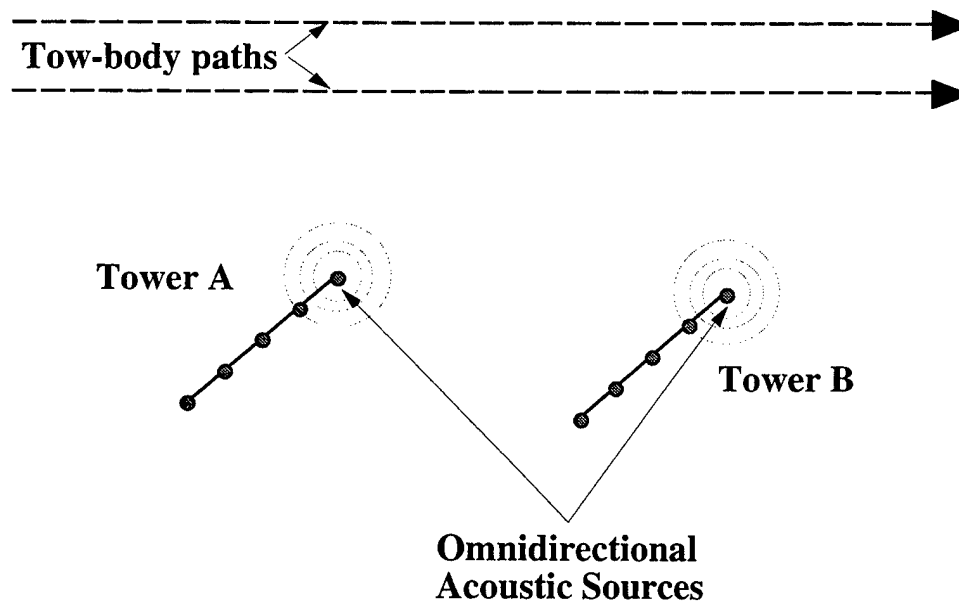
Figure 1: A schematic plan view of the experimental configuration.

The experimental runs are listed in Table I. This table shows the run number, date, and estimated distance of the track from the towers for each run where both acoustic and tow-body position data were acquired. Each run consists of two channels of data corresponding to the two receiver arrays on the tow-body. Not all of the recorded data in the runs listed in Table I was suitable for analysis, since some runs were conducted for engineering and test purposes. Section IV below includes more information about the criteria for determining which runs were appropriate for analysis.

Run Number	Date	Estimated Distance
1	8/23/96	50 m
2	8/23/96	100 m
3	8/23/96	150 m
6	8/25/96	300 m
8	8/25/96	400 m
10	8/26/96	50 m
11	8/26/96	100 m
13	8/26/96	150 m
14	8/26/96	200 m
15	8/26/96	100 m
16	8/26/96	200 m

Table I: Summary of experimental runs. Run numbers where acoustic or tow-body position data were not acquired have been omitted.

III. Data Collection

This section will discuss the acoustic, navigation, velocity, acceleration, and attitude data collected, as well as the means by which they were recorded. Example plots for each kind of data will be given from run 11, receiver array (channel) 1, and the tower designated A.

The acoustic data consist of a series of 1 ms long pulses transmitted from each of the source towers. The receiver arrays are phased-beam "doily" arrays developed by ARL/PSU, which can produce steered beams without conventional beamforming electronics. However, they were used in the normal phased-array manner with a 40° downward-looking beam. These downward-look-

ing array beams greatly limited the useful range over which acoustic data could be collected. The received acoustic signals were quadrature-sampled at 80 kHz for all runs except for runs 1–3, in which the data were base-banded to 10 kHz and sampled at 40 kHz. An example of a received acoustic pulse is shown in Figure 2 below.
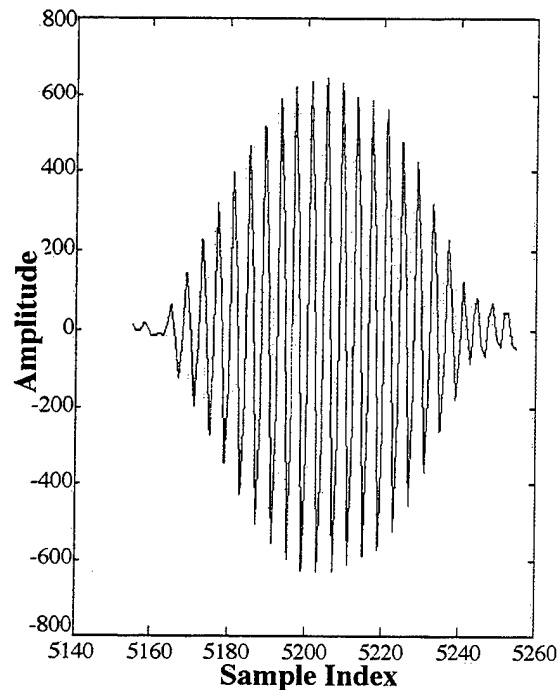
Figure 2: The received acoustic pulse from channel 1 (the first array) at the closest point of approach to the tower A for run 11.

Although the signal shown in Figure 2 has a very high signal-to-noise ratio (SNR), the received signal usually degrades rapidly due to the received beam pattern. However, using correlation techniques, as many as 100 pings of acoustic data was used on either side of the CPA. Figure 3 below gives a summary of the data for channel 1 during run 11. The upper graph shows the maximum acoustic amplitude for each ping received. This shows two peaks when the receiver array passed each tower. The lower graph shows the number of samples after the start of the received data record (a fixed time after the source pulse occurs) where these maxima were observed, and shows two parabola with minima at the points of closest approach to each tower.

Appendix A contains similar plots for all runs and channels, together with portions of the runs

magnified for easier inspection.
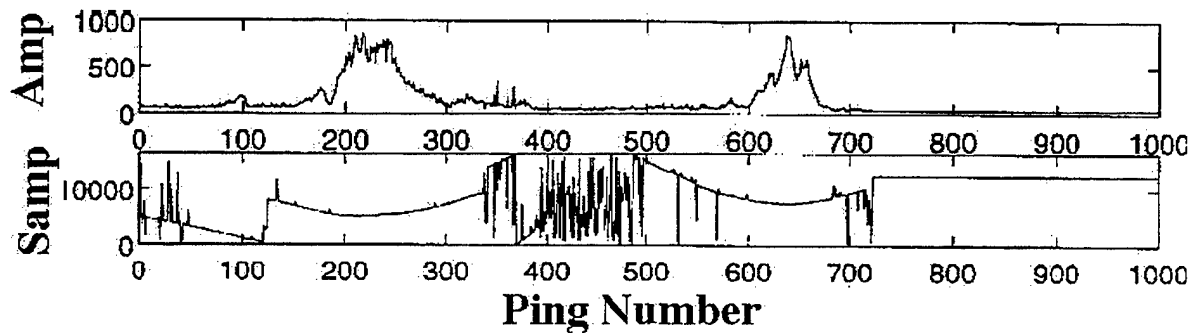
Figure 3: A summary of the acoustic data for run 11, channel 1. Plotted are maximum acoustic amplitude (top) and arrival time sample (bottom) vs. ping number for the entire run.

Tow-body velocity data were collected using an EDO Corporation, Model 3050, Doppler

Velocity Log (DVL), which records Doppler velocity measurements relative to either the water

mass or the ocean bottom at 1 sec intervals. The velocity measurements for this analysis were

made with respect to the flat ocean bottom. The DVL was mounted on the tow-body so that

measurements of the forward tow-body speed were defined to be the +X-direction and the

starboard sideways speed was defined as the +Y-direction of a body-fixed coordinate system.

The vertical (Z-direction) motion of the tow body was not measured and will be taken as zero.

An example of these data is shown in Figure 4 below for run 11. For most of the run, the X-

velocity is approximately 1 m/s and the Y-velocity is approximately 0.2 m/s. The large

anomalies shown between 500 and 700 seconds are due to navigational maneuvers of the tow

ship. These anomalies are also evident in other recorded motion data such as the acceleration and

rotational measurements shown in Figure 5.
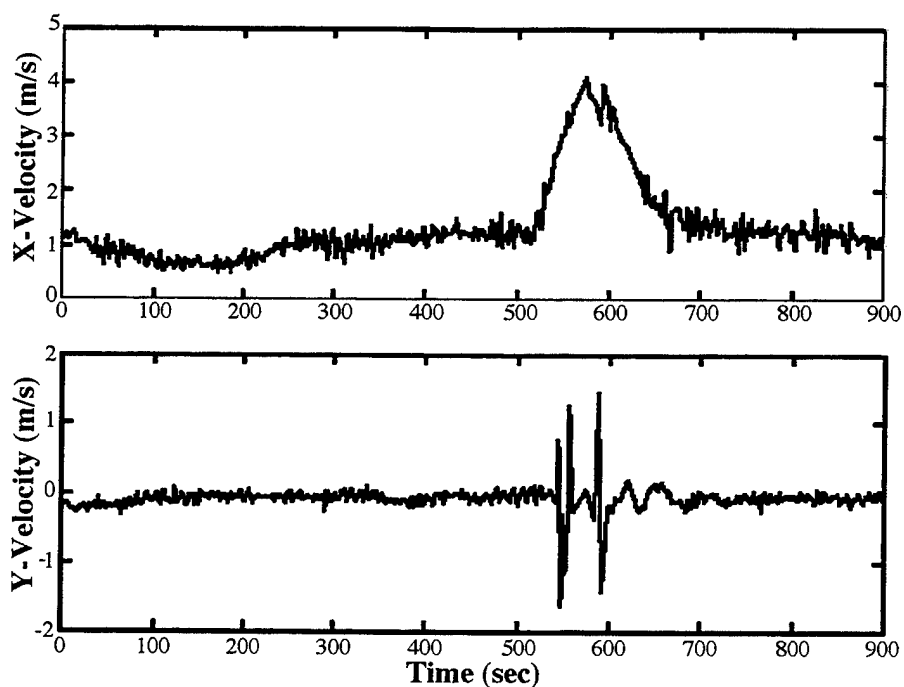
Figure 4: Velocity measurements relative to the flat bottom for run 11. Positive X and Y are forward and starboard, respectively. No Z velocity measurements were made.
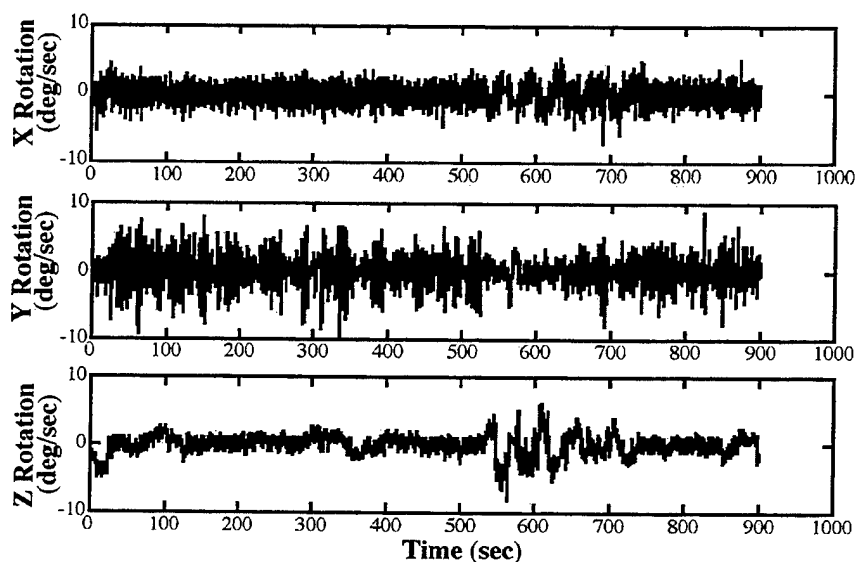
Figure 5: Angular rotation rate measurements for run 11.
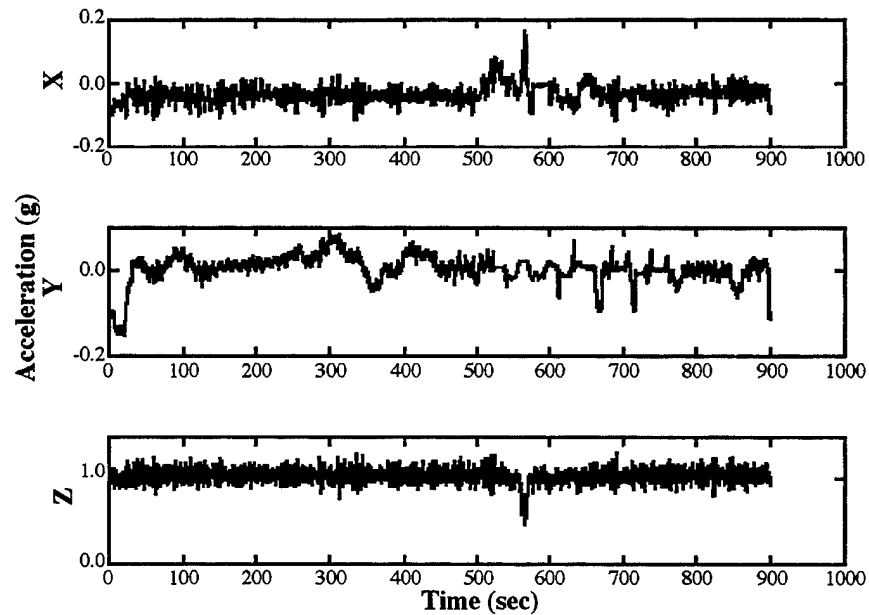
Figure 6: Linear acceleration for run 11 along the X-, Y-, and Z-axes.

Tow-body acceleration was measured using a Systron Donner Motion Pak sensor, Model

No. MP-GCCCQVVV-100, which provides two types of measurements sampled at 10 Hz. The

first (see Figure 5 above) is the angular rate of rotation about the 3 axes of an orthogonal,

rectangular coordinate system fixed in the body (forward, starboard,and up corresponding to

positive X, Y, and Z, respectively). The second (see Figure 6 above) is the linear acceleration of

the tow-body along the same 3 axes. The constant 1-g acceleration bias in the Z-direction is due

to gravity.

Attitude measurements were also made using an Electronic Compass Module, Model TCM2, made by Precision Navigation. This device provides measurements of the heading, pitch, and roll, sampled at 10 Hz. An example of these data for run 11 is shown in Figure 7.
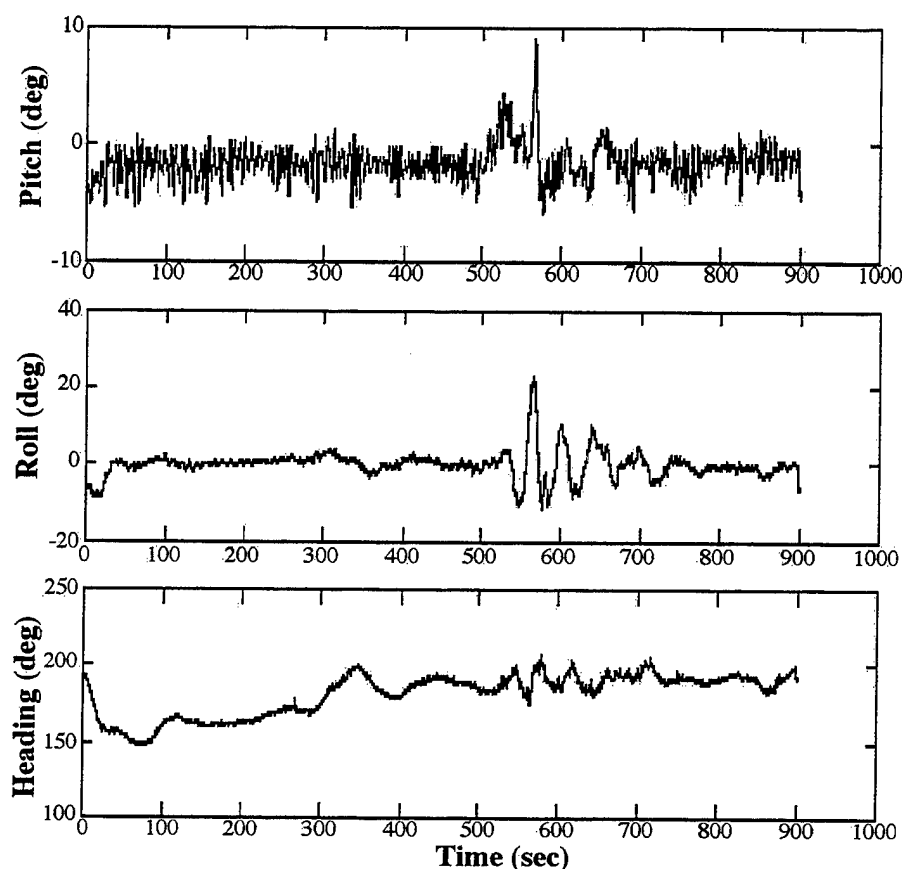
Figure 7: Attitude sensor measurements for run 11.

Since NRL's towed vehicle has a very large mass inertia, the spatial path of the receiver arrays may be assumed linear over short distances, or, equivalently, short time intervals. The velocity (Figure 4), angular rotation rate (Figure 5), linear acceleration (Figure 6) and attitude (Figure 7) measurements discussed bear this out, since they show only small changes between pings (i.e., 1 second intervals).

IV.   Acoustical Data Analysis

In this section, the method for determining phase fluctuations will be discussed. Run 11, channel 1, tower A will again be used for illustration. The results of analysis for all runs will be discussed more fully in Section VI.

Phase adjustments are applied to the tow-body flight path to achieve an equivalent, spatially linear track. This procedure involves adjusting the arrival time of each received acoustic signal along the flight path until they are those of the linear track. Beamform processing over the resulting linear aperture can then be compared to results for the same aperture in a constant velocity medium. The difference in the resulting beam patterns is representative of the effect of environmental fluctuations present in the water column.

As discussed in Section III above, the tow-body flight path may be considered approximately linear between ping arrivals. If the path is linear and the velocity constant, then arrival time is a quadratic function of ping number. In this case, a best-fit parabolic path over a small number of contiguous arrival times corresponds to a linear best-fit curve through the receiver positions for those arrivals. Therefore, the deviations of the received acoustic signals from the best-fit parabolic path (i.e., the linear spatial flight path) is a measure of the ping-to-ping variation induced by the environment.

There are rather stringent accuracy requirements on the determined receiver positions. The accuracy required is inversely proportional to the acoustic frequency. For example, a 20 kHz signal in a medium with a nominal phase velocity of 1490 m/s will have a wavelength of about 7.5 cm. If phase variations on the order of $10°$ are to be detected, the receiver position must be determined to within 0.21 cm. Although no direct measurements of the tow-body location along its flight path were made, the required accuracy is obtained through temporal means. The received

acoustic signals were sampled at 80 kHz and recorded on optical disks. The oscillator providing the sampling rate is highly stable to an accuracy of 0.0005% of the sampling frequency, a timing accuracy of 6.25 x 10^{-11} seconds. The arrival time for each ping is accurately and consistently identified by tracking the maximum of the correlation function between the envelope function of a synthesized version of the transmitted waveform (the actual transmitted signal was not measured) and the envelope function of the received waveform. (Leading-edge and trailing-edge waveform detection were impractical due to, at times, low SNR.) FFT interpolation is used to improve interpolation accuracy results beyond the resolution of the sampled data, achieving a time resolution of 0.4 μs or 2.8° of phase. Further, if the correlation coefficient between the envelopes of the two waveforms is less than 0.7, the data is deemed unacceptable for processing.
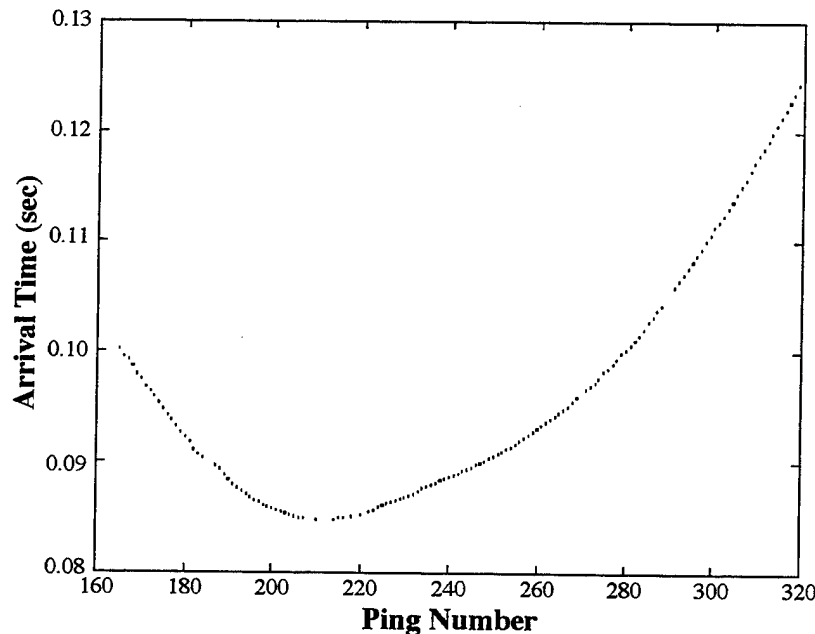
Figure 8: Arrival time vs. ping number (1 ping per second) for run 11. Each point corresponds to an arrival time calculation. Missing points indicate data deemed not acceptable for processing.

An example of the results of this technique is shown in Figure 8, with the acoustic arrival time plotted as a function of ping number. Each point on the graph in this figure represents an

arrival of an acoustical signal. Gaps correspond to arrivals whose correlation coefficient with the source waveform was below 0.7.

Fitting of a small set of arrival times (e.g. 6 points) to a quadratic polynomial (corresponding to a linear spatial track) is done contiguously along the track. The temporal fluctuations from the average fitted-track are then calculated by subtracting the acoustic arrival time from the fitted-track at that point. An example of the results of these calculations is shown in Figure 9, showing the time fluctuations along a spatially linear path.
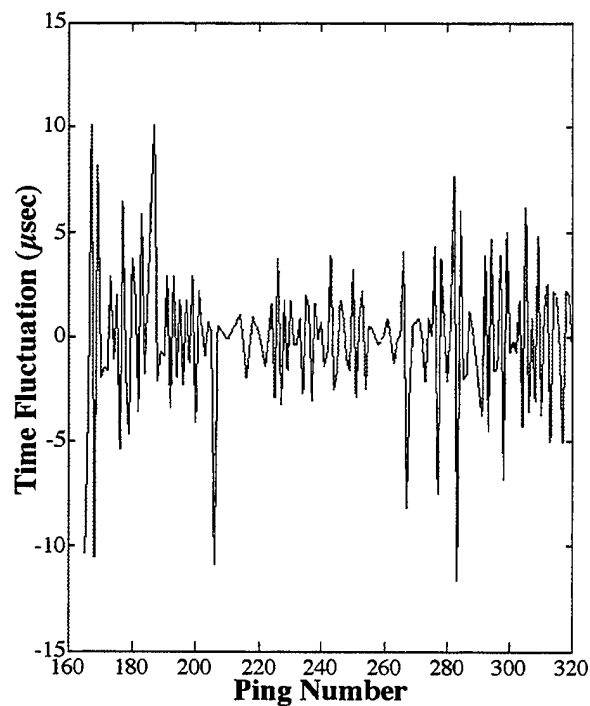
Figure 9: **Time fluctuations along the towpath for run 11 as calculated from the arrival time structure illustrated in Figure 8.**

The changes in the sound speed required to produce the calculated fluctuations will now be determined to see whether the changes in temperature, salinity, and currents, (hence, sound speed) can reasonably be of such magnitude that the observed time fluctuations are found. Sound speed in the ocean is a function of temperature, salinity, and depth and is given by:[1]

$$c = 1449 + 4.6T - 0.55T^2 + 0.003T^3 + (1.39 - 0.012T)(S - 35) + 0.017z \qquad (1)$$

where c is the sound speed in meters/second, T is the temperature in degrees Celsius, S is the salinity in parts per thousand, and z is the depth in meters. Eq. (1) indicates that sound speed is much less sensitive to changes in salinity and depth than to changes in temperature, so salinity and depth will be ignored in our first-order approximation.

It can be shown to first-order that the ratio of the time fluctuations to the arrival time is proportional to the corresponding change in sound speed to a reference sound speed. That is, if $c = \dfrac{D}{t}$ where c is the sound speed, D is the path length, and t is the travel time, then

$$\frac{\Delta t}{t} = -\frac{\Delta c}{c}. \qquad (2)$$

The reference speed c_0 used in all calculations which follow is 1490 m/s, and is representative of the average sound speed in the experimental area as found from measured sound speed profiles. This corresponds to a temperature T_0 of about 10°C.

Once Δc is found, the associated change in temperature ΔT may be calculated using Eq. (1). For temperatures near T_0, the second and third order terms in T are quite small (5.5 m/s and 3 m/s, respectively), hence these terms may be neglected in determining ΔT. The value of ΔT is calculated as (see Figure 10 below)

$$\Delta T = T - T_0 = \frac{(c_0 + \Delta c) - 1449}{4.6} - \frac{c_0 - 1449}{4.6} = \frac{c_0\left(1 + \dfrac{\Delta t}{t}\right) - 1449}{4.6} - \frac{c_0 - 1449}{4.6}. \qquad (3)$$
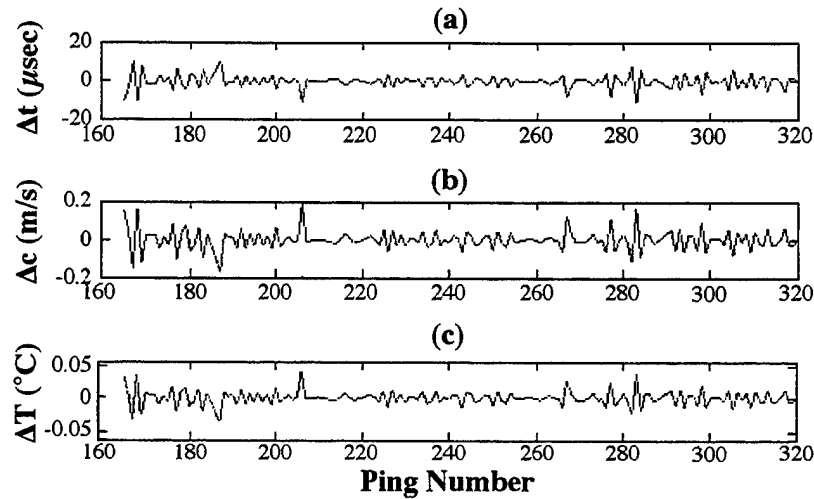
Figure 10: From the time of flight fluctuations [plot (a), see Figure 9] and the total transit time [see Figure 8], Δc is determined by Eq. (2) [plot (b)]. Temperature fluctuations are obtained from Eq. (3) [plot (c)]. The data is from run 11, channel 1, tower A.

Finally, the time fluctuations are converted to phase variations that are shown in Figure 11.

How one might interpret these phase variations in terms of SAS system performance will be discussed in the next section.
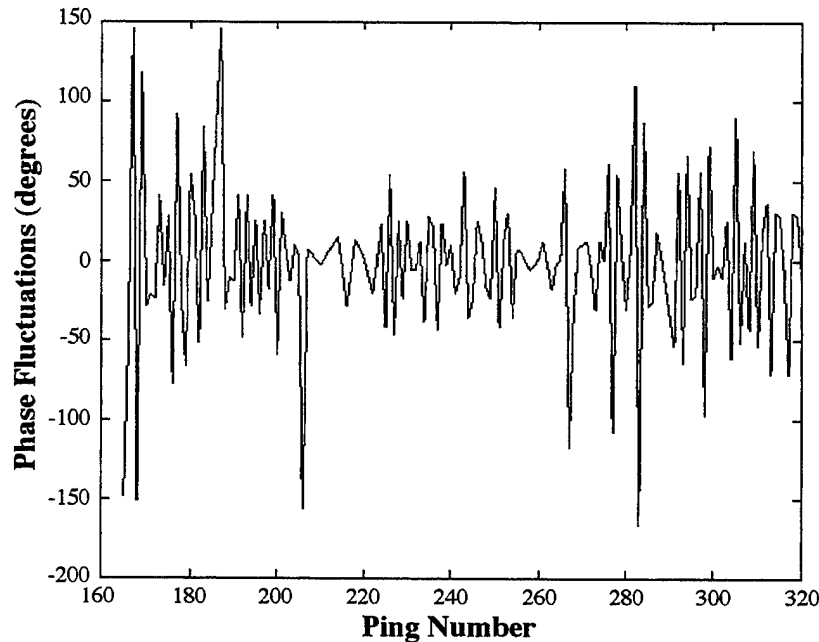
Figure 11: Calculated phase fluctuations for run 11, channel 1, tower A. The standard deviation of the fluctuations is 51.50° and the mean value is −2.017°.

V. Array Performance Theory

As discussed at the beginning of Section IV, one can model a synthetic aperture array as a linear, spatial array to gain insight into SAS performance in the presence of these signal phase variations. Since this experiment used one-way signal propagation, the measured phase errors are doubled to reflect comparable SAS operations, which use two-way propagation.

The following theory for linear arrays follows Shifrin[2]. Consider a linear array of length L lying along the z-axis between $z = -L/2$ and $z = +L/2$ so that the phase of the signal at the receiver at point z is $\phi(z)$. If $\phi(z)$ is a zero-mean random variable with standard deviation $\sigma(z)$, then the correlation coefficient can be written

$$r(z, z_1) = \frac{\langle \phi(z)\phi(z_1) \rangle}{\sigma(z)\sigma(z_1)}.$$

A correlation length ρ may then be defined by assuming $r(z, z_1)$ has the form of a Gaussian

$$r(z, z_1) = \exp\left[-\frac{(z - z_1)^2}{\rho^2} \right].$$

The relative coordinates $x \equiv 2z/L$ and the correlation length in relative units $d \equiv 2\rho/L$ may also be defined. Shifrin gives the mean power of the beam pattern I for a linear array as a function of $\sigma(z)$:

$$\langle |I(\psi)|^2 \rangle = e^{-\sigma^2}\left[\left(\frac{\sin\psi}{\psi} \right)^2 + \frac{1}{4}\sum_{m=1}^{\infty} \frac{\sigma^{2m}}{m!} I(d_m, \psi) \right], \tag{4}$$

where ψ is the generalized angle $\psi = \frac{\pi L}{\lambda}\sin\theta$, θ is the angle measured normal to the array, λ is the signal wavelength,

$$I(d_m, \psi) = \int_{-1}^{+1}\int_{-1}^{+1} e^{-\frac{(x-x_1)^2}{d_m^2} + i\psi(x-x_1)} \, dx\,dx_1,$$

---

and $d_m \equiv \dfrac{d}{\sqrt{m}}$. Without phase errors, the average power of the beam pattern is represented by the

first term in Eq. (4). The remaining terms yield the changes to the beam pattern caused by the

phase errors.

Consider some examples. In all cases, the array length L will be 200 m, and the sample points

will be spaced 2 m apart, that is, the SAS is pinged 100 times at 2 m intervals.
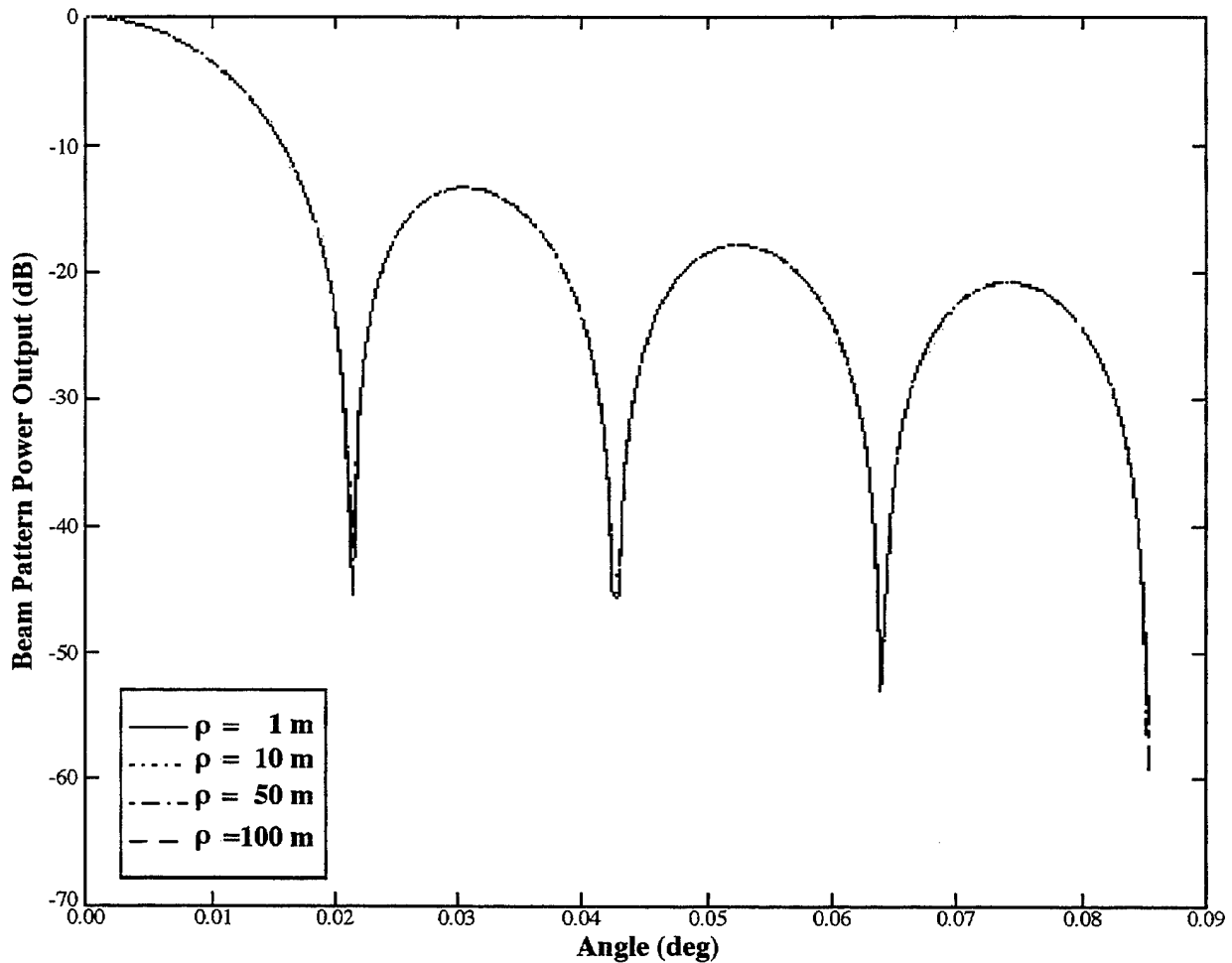
Figure 12: **The effect of correlation length ρ on beam pattern power. In all cases,
the standard deviation σ of the phase was 1°. The power was plotted in
dB relative to the maximum value at $\rho = 0$.**

The effect of varying the correlation length ρ while keeping the standard deviation of the

phase error at a constant 1.0° is shown in Figure 12. The mean power of the beam pattern for

ρ = 1, 10, 50, and 100 m (relative correlation lengths d of 0.01, 0.1, 0.5, and 1.0, respectively) are plotted as a function of angle. The maximum angle plotted corresponds to $\psi = 4\pi$. Note that despite a change in correlation length of two orders of magnitude, the beam pattern appears nearly unchanged.
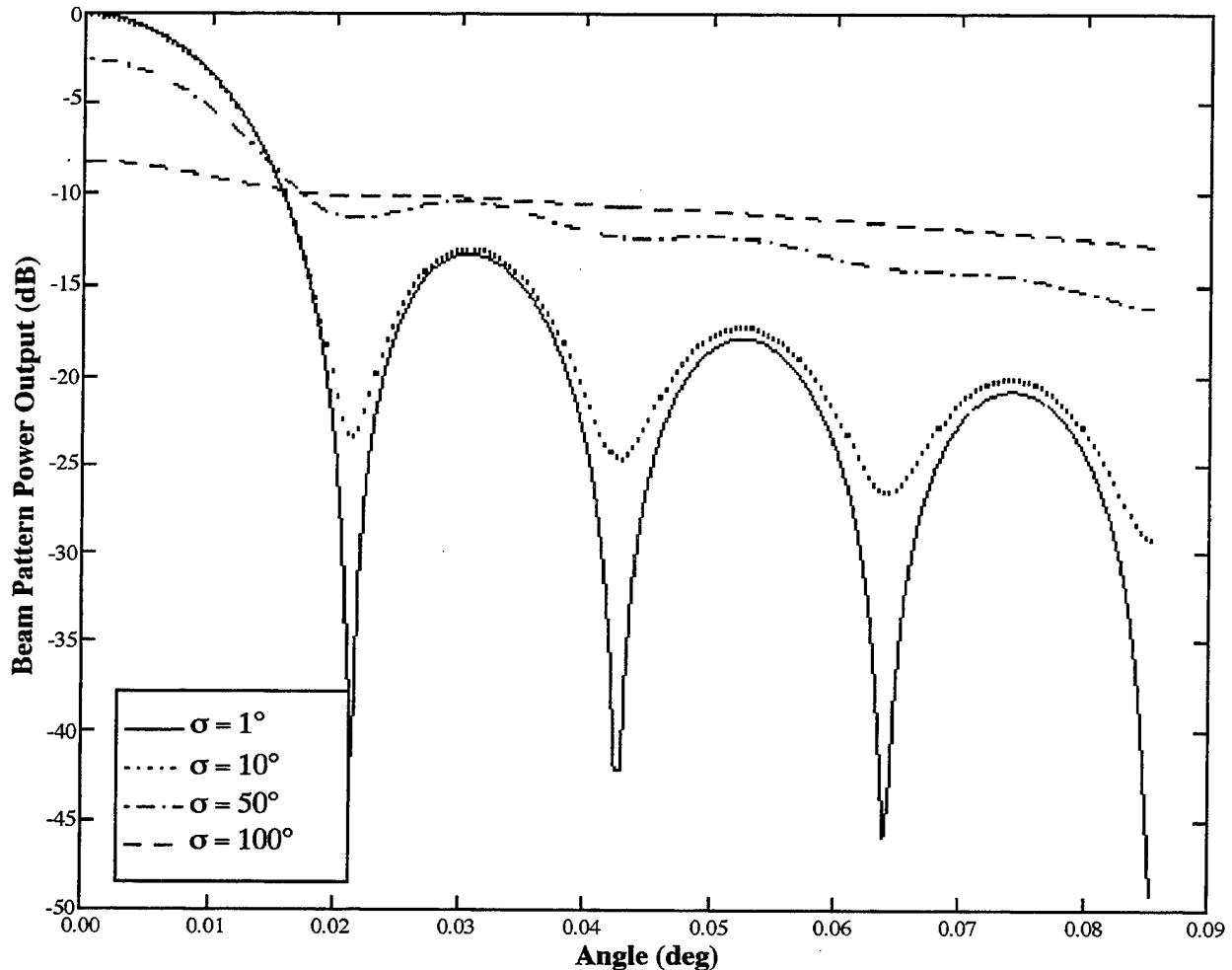
Figure 13: The effect of phase error standard deviation σ on beam pattern power. In all cases, the correlation length ρ of the phase was 20 m (0.2 in relative units). The power was plotted in dB relative to the maximum value at $\sigma = 0$.

The effect of varying the standard deviation of the phase error is shown in Figure 13, keeping the correlation length ρ at a constant 20 m (0.2 in relative units). Here, significant beam pattern

degradation can be seen. There are some effects for $\sigma = 10°$, much more significant degradation of the beam pattern at $\sigma = 50°$, and near loss of the beam pattern at $\sigma = 100°$.

VI. Results

This section expands the analysis in Sections IV and V to include all of the experimental data chosen for analysis. Data are given for run 10 (channel 1, tower A), run 11 (channels 1 and 2, towers A and B) and run 13 (channel 1, tower A). These runs were chosen because most of the collected data from them was usable in the analysis, i.e. the correlation coefficient between the envelope functions of the transmitted and received waveforms was greater than 0.7 for the vast majority of the acoustic data in the run. In Section VI.A, plots similar to Figure 8 showing arrival time as a function of ping number will be given for each run. Section VI.B contains plots showing the variations in flight time, sound speed, and temperature for each run (see Figure 10). Plots like Figure 11 of the phase variations for each run are given in Section VI.C. And finally, in Section VI.D the simulated beam patterns of actual and ideal results for each run are given for comparison.

For the sake of brevity, runs will be denoted as *run.channel-tower*. For example, run 10, channel 1, tower A will be written run 10.1-A.

A. Acoustic Time of Flight

The acoustic flight times, plotted in Figures 14–19 below, were calculated using the technique described at the beginning of Section IV (see Figure 8). All the data have the expected rough parabolic shape, corresponding to a roughly linear spatial track. As in Figure 8, each point on the plots corresponds to a time of flight calculation. Data for which the correlation coefficient between the envelope functions of the transmitted and received waveforms were greater than 0.7

are excluded from the plots. Figure 14 is identical to Figure 8 and is included only for convenient comparison of the data.

It is difficult to examine these plots and discriminate between large and small phase errors. The plots in the next subsection will make this process easier.
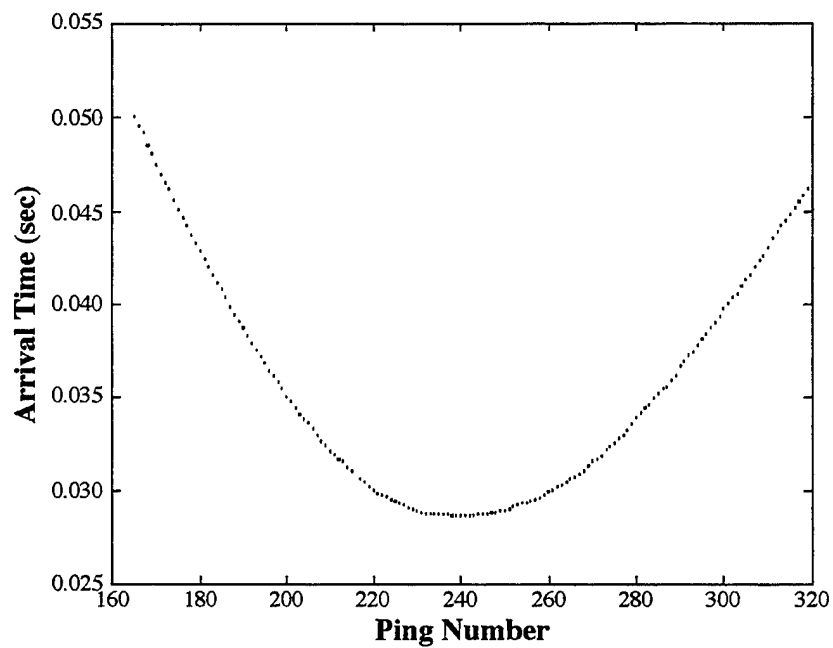
Figure 14: Acoustic time of flight for run 10.1-A.
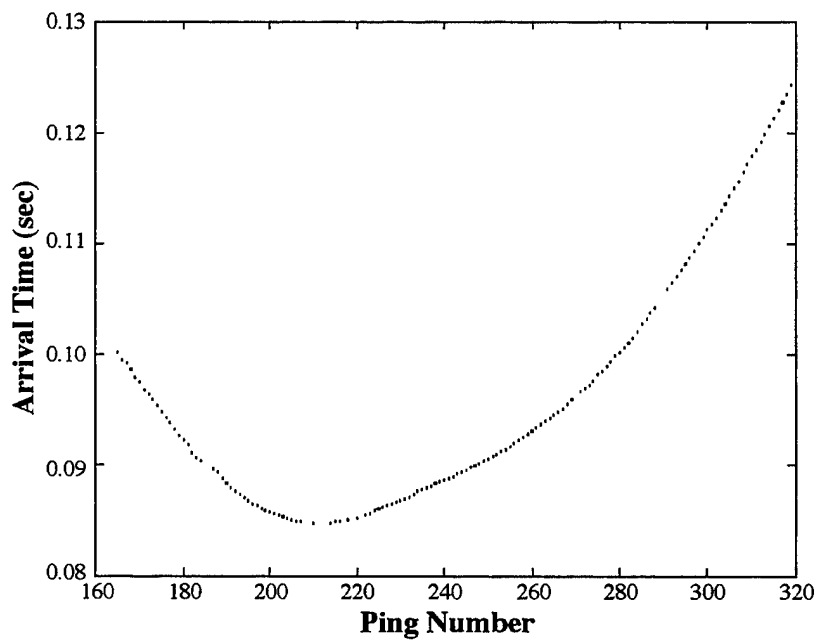
Figure 15: Acoustic time of flight for run 11.1-A.
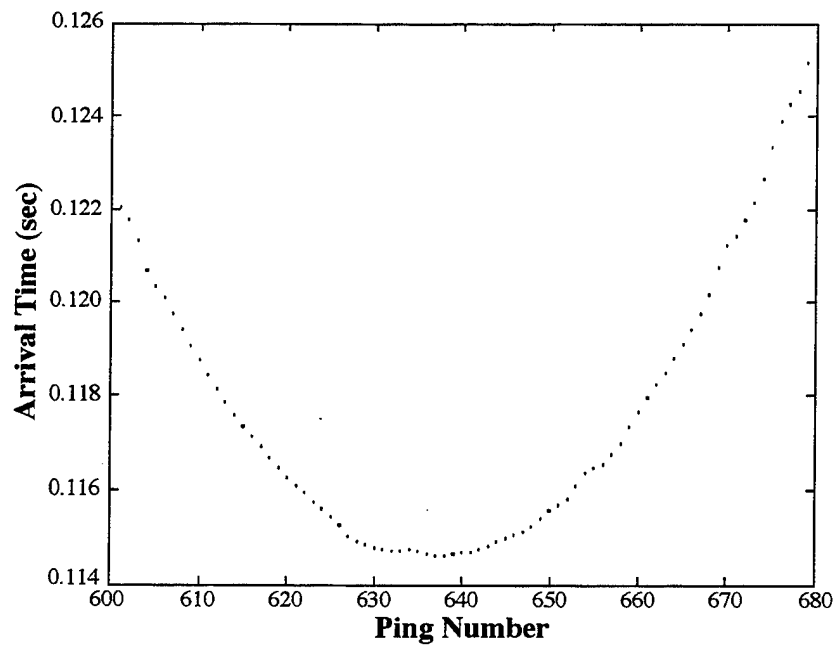
Figure 16: Acoustic time of flight for run 11.1-B.
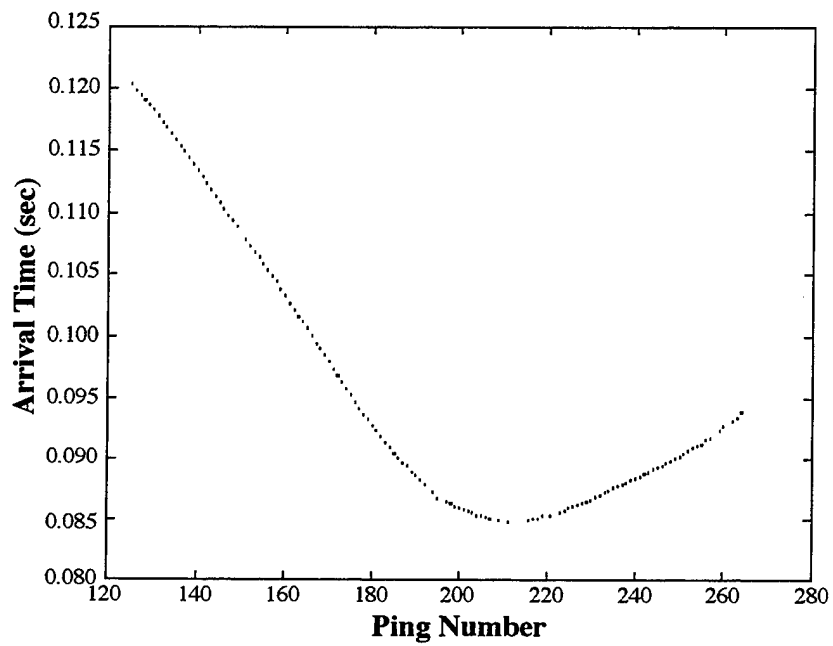
Figure 17: Acoustic time of flight for run 11.2-A.
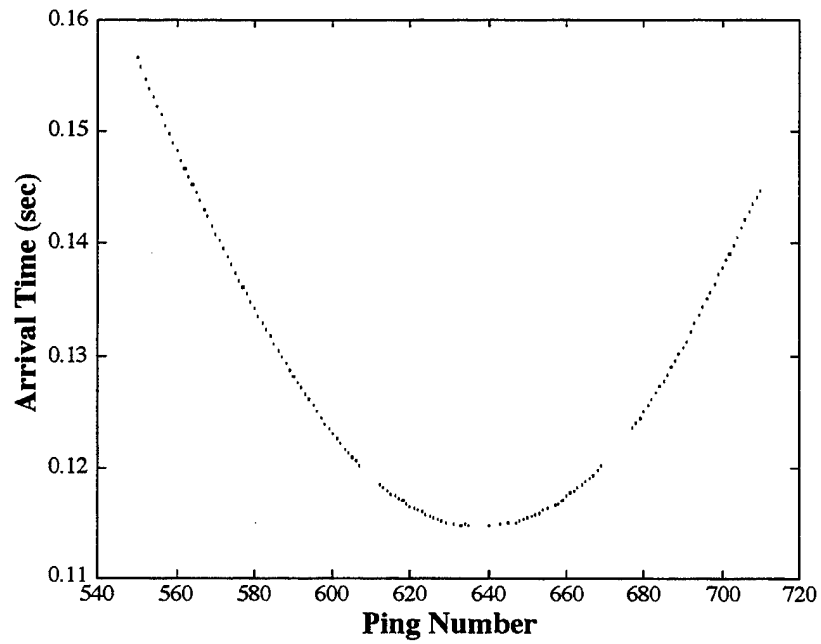
Figure 18: Acoustic time of flight for run 11.2-B.
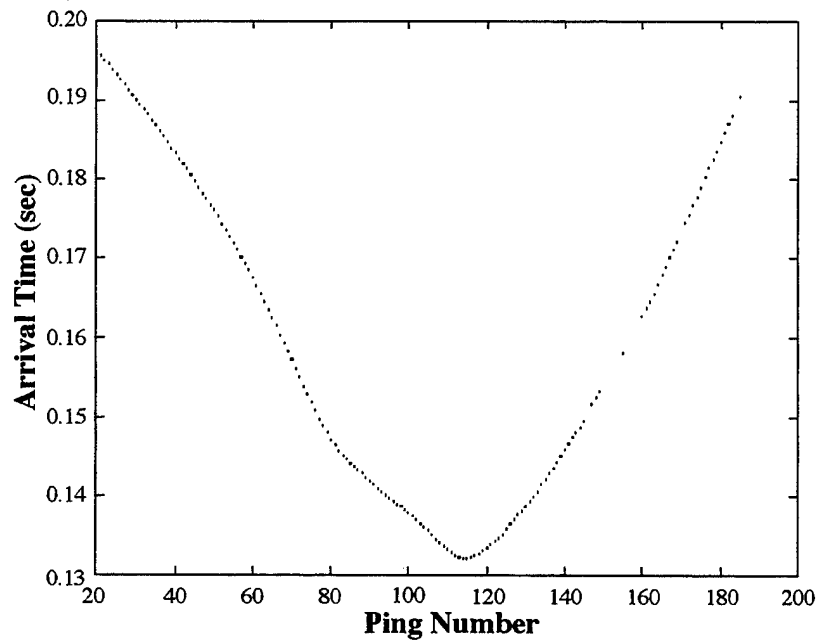
Figure 19: Acoustic time of flight for run 13.1-A.

B. Flight Time, Sound Speed, and Temperature Variations

The variations in acoustic flight time, sound speed, and water temperature, calculated using the technique described in Section IV (see Figure 10), are plotted in Figures 20–25 below. In each figure, plot (a) shows the absolute time of flight fluctuations in μsec, plot (b) shows the calculated sound speed fluctuations in m/s, and plot (d) shows the calculated temperature fluctuations in Celsius degrees.

Note that the largest temperature fluctuations (on the order of tenths of a Celsius degree) are found in runs 10.1-A (Figure 20), 11.1-B (Figure 22) and 11.2-B (Figure 24). Smaller fluctuations (on the order of hundredths of a Celsius degree) are found in the remaining plots (Figures 21, 23, and 25). These temperature fluctuations of course correspond to phase variations, as will be seen in the next subsection.
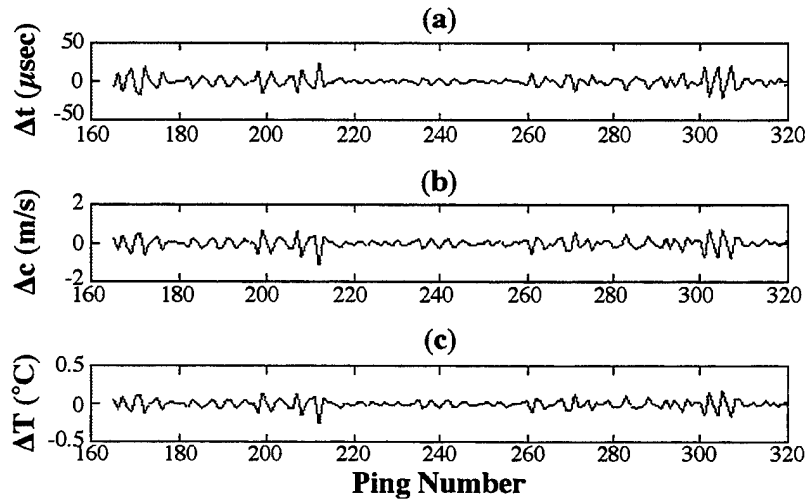
Figure 20: Flight time, sound speed and temperature fluctuations for run 10.1-A.
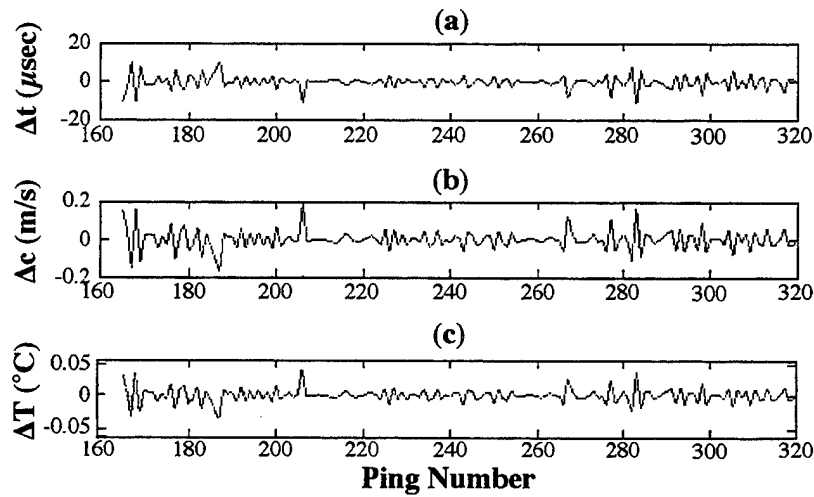
Figure 21: Flight time, sound speed and temperature fluctuations for run 11.1-A.
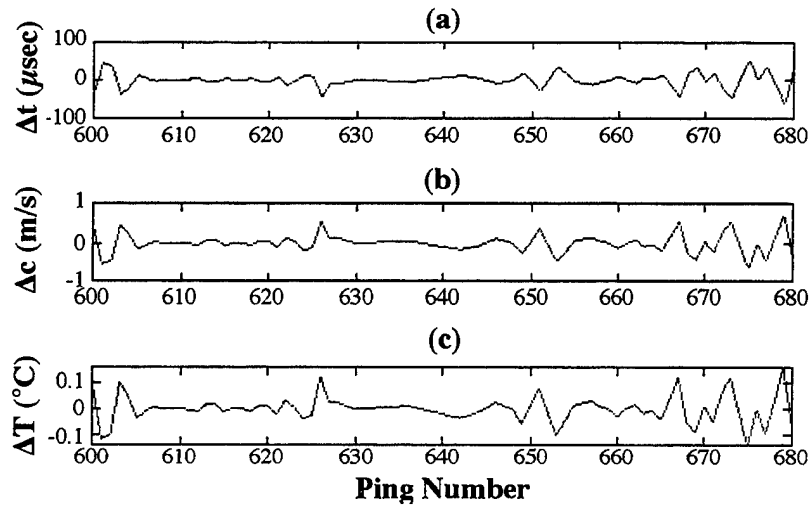
Figure 22: Flight time, sound speed and temperature fluctuations for run 11.1-B.
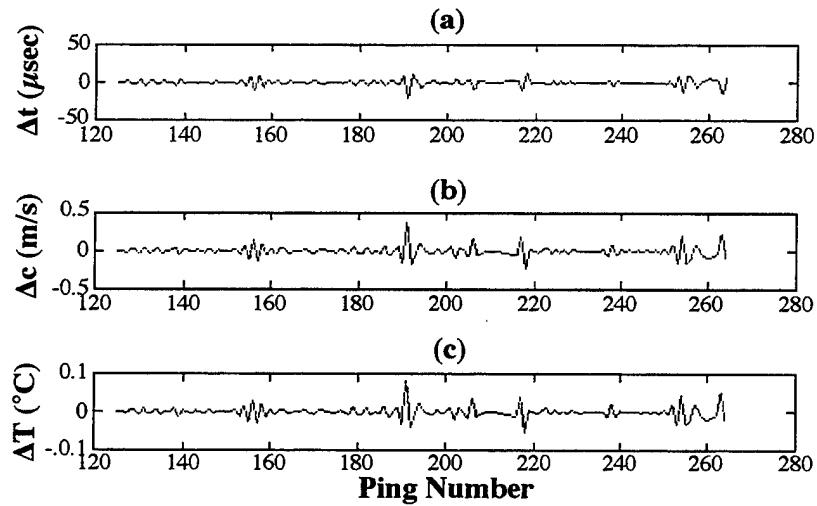
Figure 23: Flight time, sound speed and temperature fluctuations for run 11.2-A.
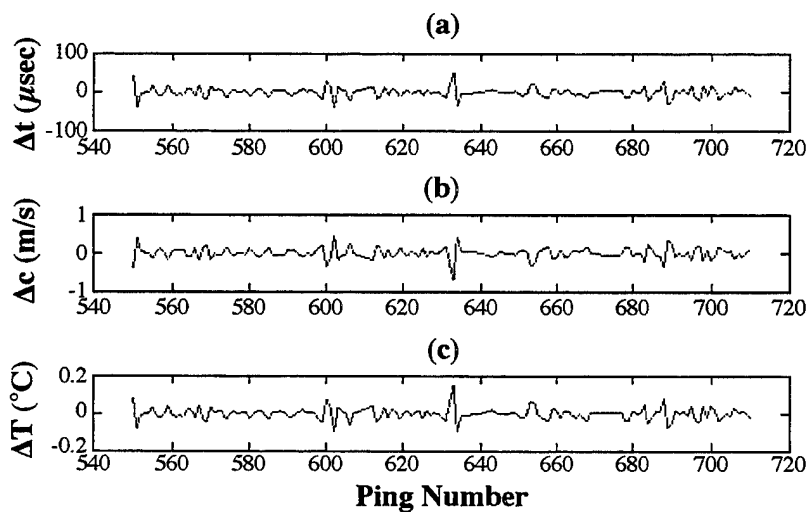
Figure 24: Flight time, sound speed and temperature fluctuations for run 11.2-B.
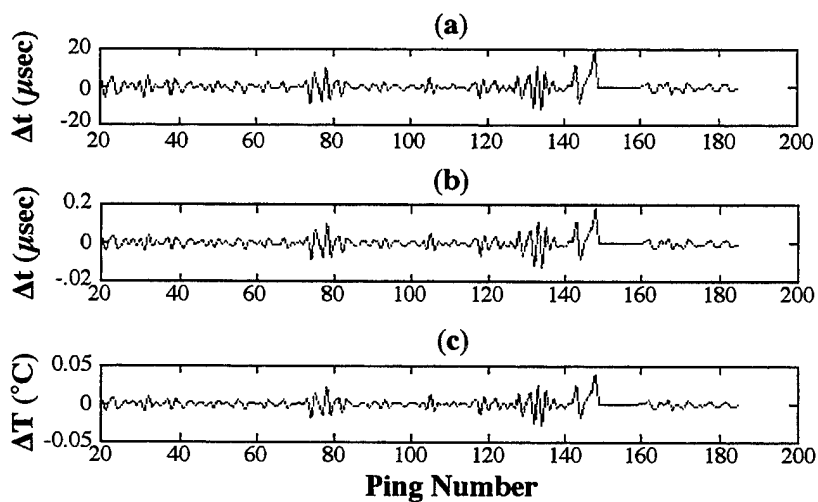
Figure 25: Flight time, sound speed and temperature fluctuations for run 13.1-A.

C. Phase Variations

The variations in signal phase, calculated from the time fluctuations in plot (a) from Figures 20–25 above (see Figure 11), are plotted in Figures 26–31 below. The mean and standard deviation of the phase variations are given in Table II below.

Run	Mean	Standard Deviation
10.1-A	-0.1661°	109.2°
11.1-A	-2.017°	51.58°
11.1-B	5.147°	300.7°
11.2-A	-0.1553°	67.69°
11.2-B	-2.409°	193.0°
13.1-A	2.669°	57.17°

Table II: Phase fluctuation statistics for the analyzed runs.

As expected from the discussion in the previous subsection, the largest phase fluctuations occur in runs 10.1-A, 11.1-B, and 11.2-B. These fluctuations will be shown in the next subsections to have severe implications on SAS performance.
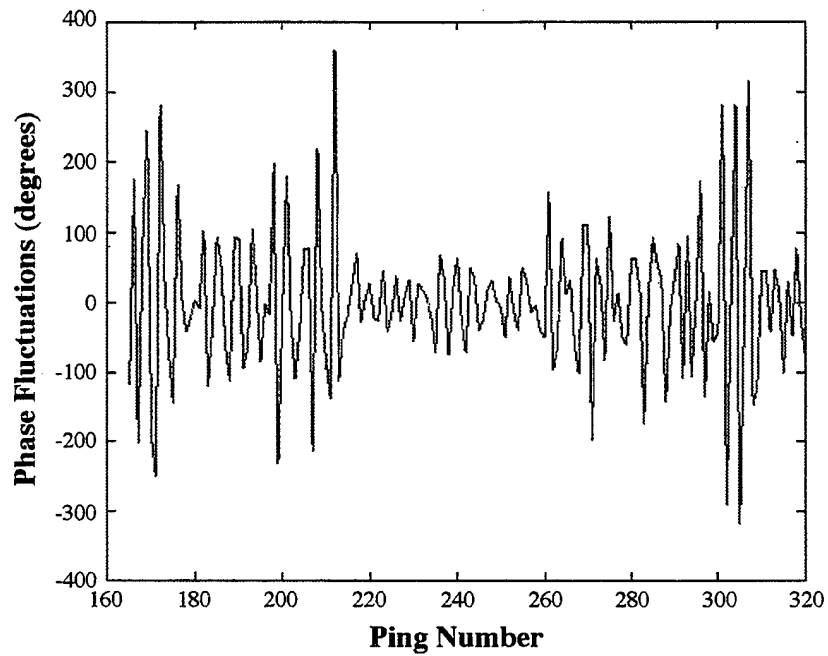
Figure 26: Phase fluctuations for run 10.1-A.
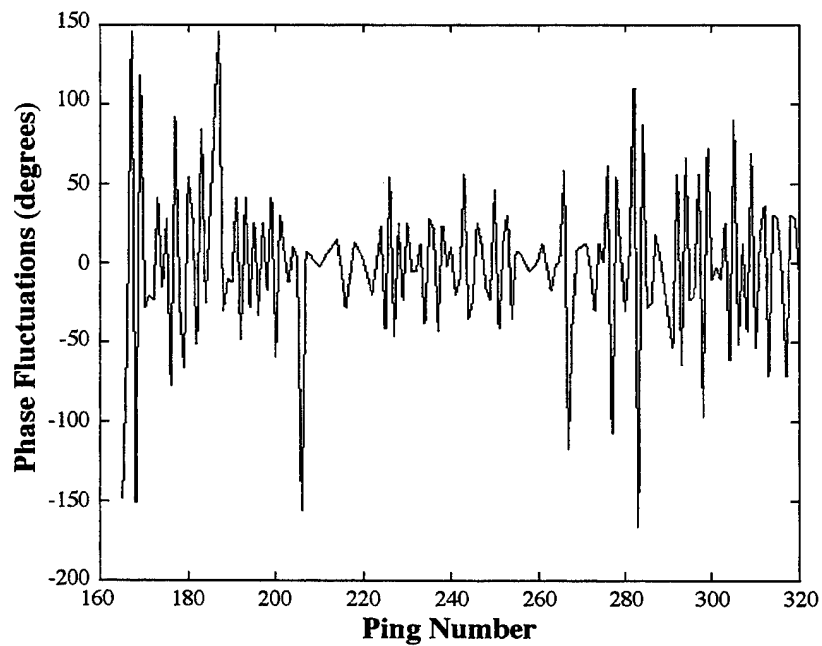
Figure 27: Phase fluctuations for run 11.1-A.
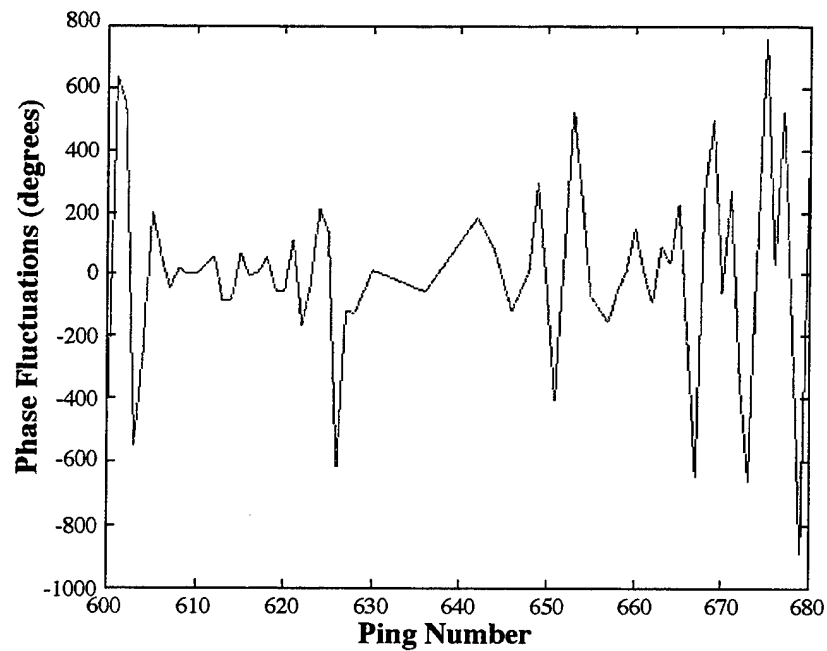
Figure 28: Phase fluctuations for run 11.1-B.
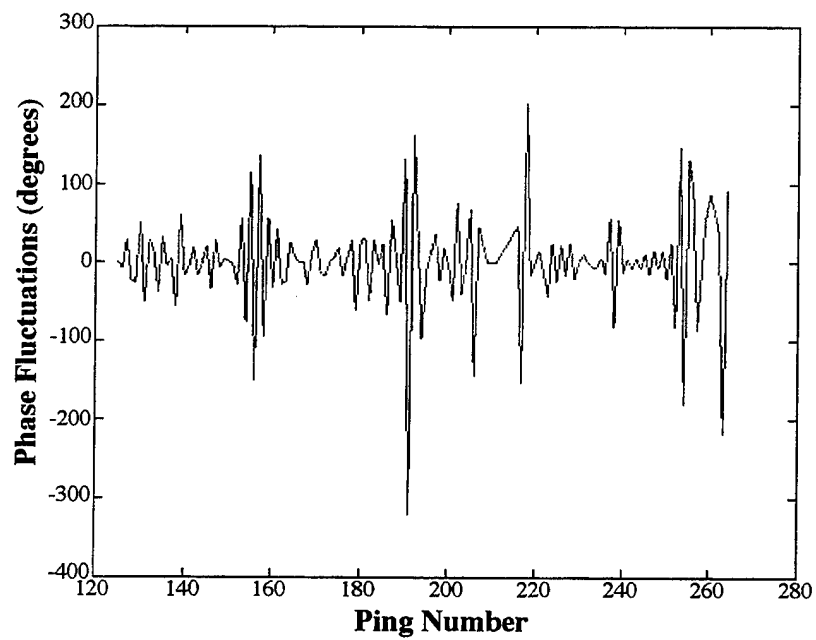
Figure 29: Phase fluctuations for run 11.2-A.
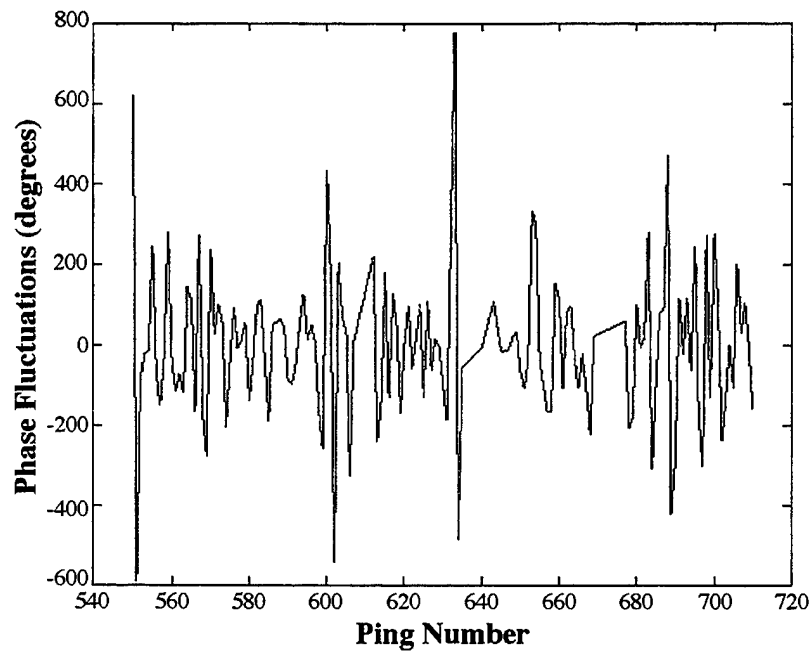
Figure 30: Phase fluctuations for run 11.2-B.
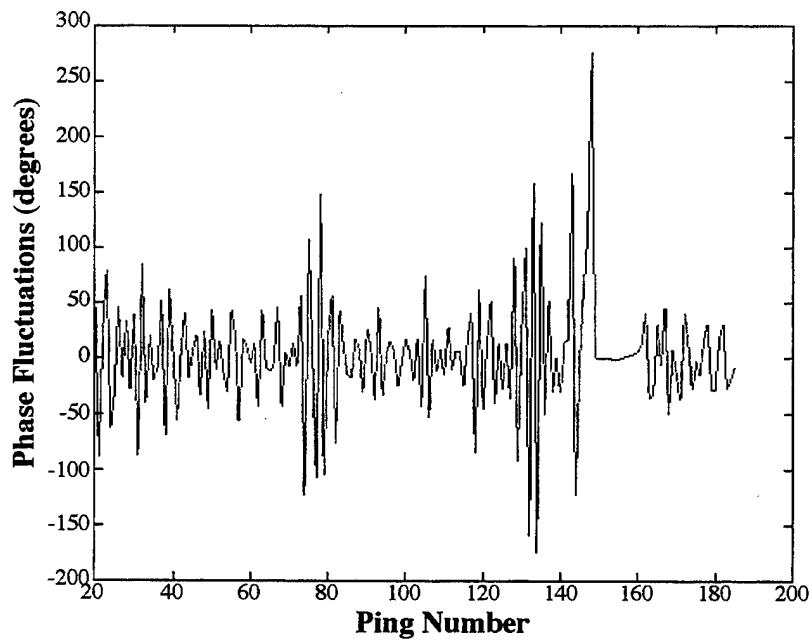
Figure 31: Phase fluctuations for run 13.1-A.

D. SAS Beam Pattern Simulations

The simulated beam patterns, calculated according to the theory in Section V, are plotted in Figures 32–37 below. The patterns are plotted in dB relative to the maximum response for the ideal case. The correlation and array lengths used are given in Table III; the standard deviations used are identical to those in Table II.

Note that the three cases with the least phase variability (Figures 33, 35, and 37) show degraded but recognizable beam patters. However, the three cases with the greatest phase variability (Figures 32, 34, and 36) show nearly omnidirectional patterns, indicating a complete loss of SAS performance. One must therefore conclude that there are some conditions where environmental variability will significantly hinder SAS performance, at least to the extent that SAS performance is modeled here.

Run	Correlation Length (m)	Array Length(m)
10.1-A	2.499	145.0
11.1-A	1.841	183.8
11.1-B	0.9813	100.0
11.2-A	2.115	157.3
11.2-B	1.240	199.0
13.1-A	2.733	285.4

Table III: Correlation and array lengths for simulated arrays.
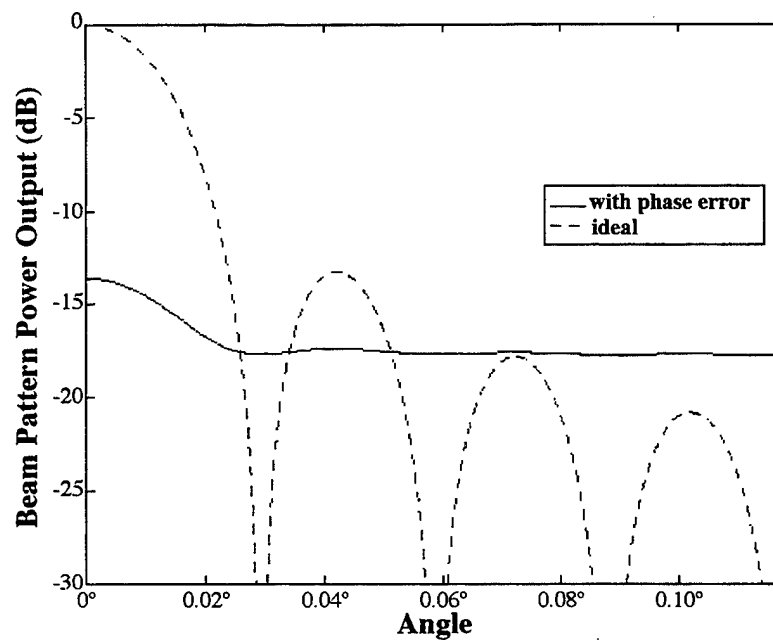
Figure 32: Simulated beam pattern for run 10.1-A.
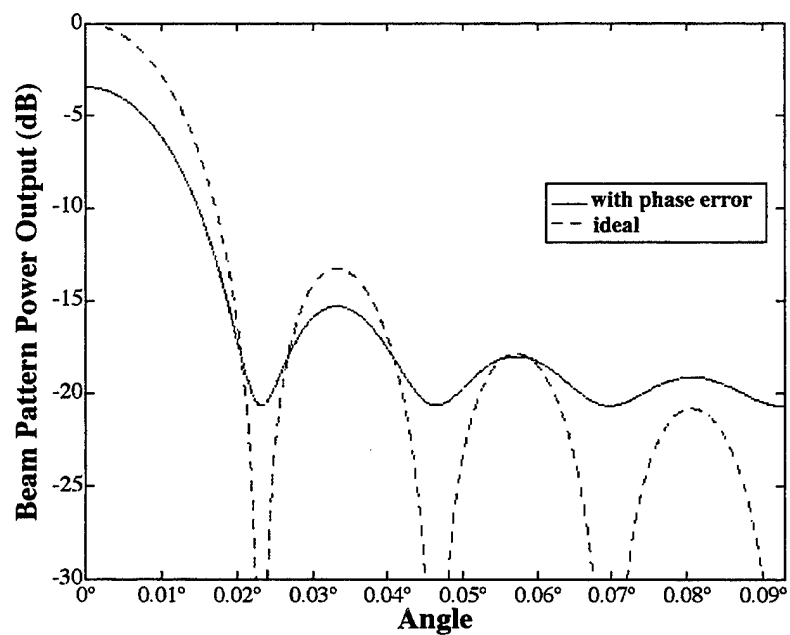
Figure 33: Simulated beam pattern for run 11.1-A.
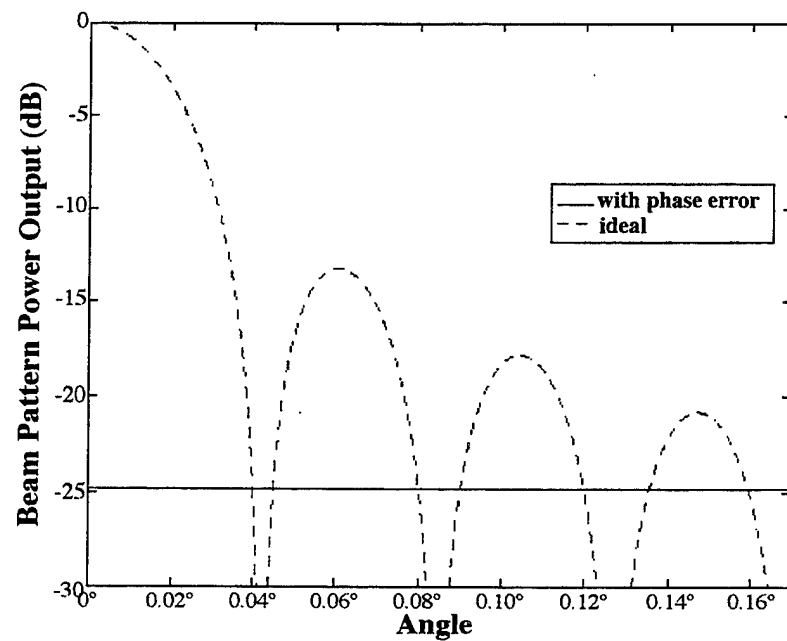
Figure 34: Simulated beam pattern for run 11.1-B.
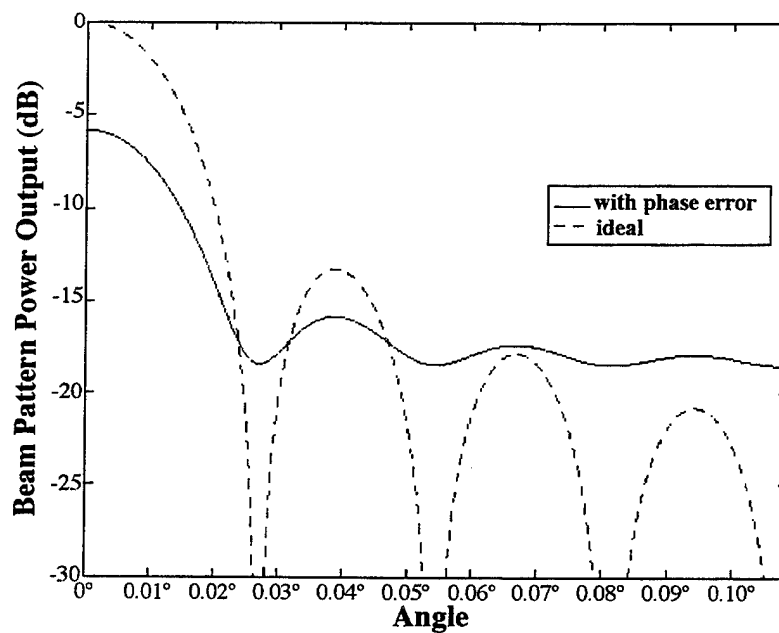
Figure 35: Simulated beam pattern for run 11.2-A.
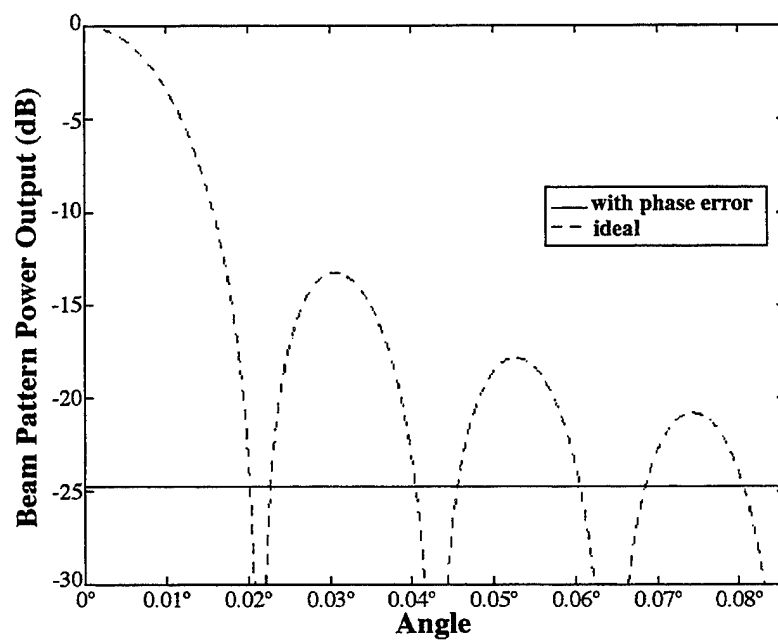
Figure 36: Simulated beam pattern for run 11.2-B.
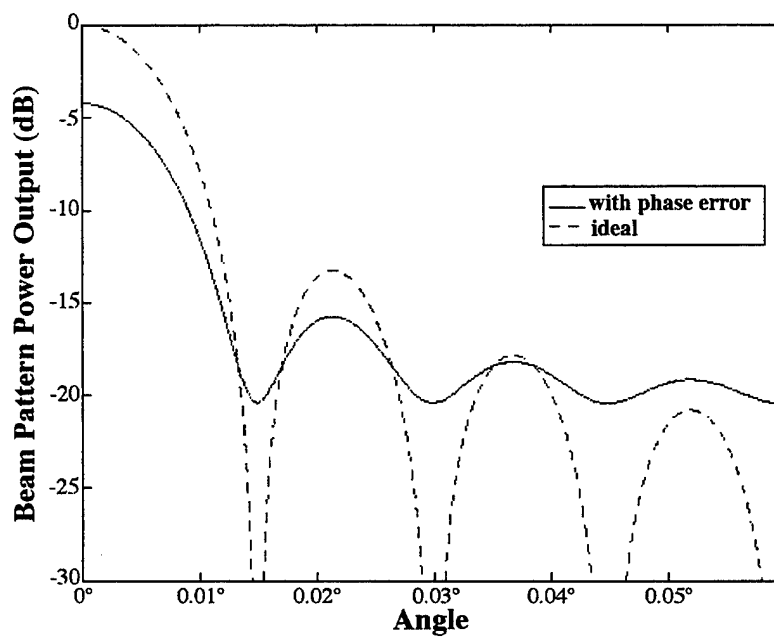
Figure 37: Simulated beam pattern for run 13.1-A.

VII. Conclusions

This paper reports on an experiment which measured acoustic signal phase fluctuations, and determines the effects that this propagation through the random ocean media might have on SAS performance. The experiment showed conditions where large-scale phase errors could significantly disrupt SAS performance, as well as conditions where performance degradation was less significant.

Of course, there is significant further research to be done. The current experiment did not involve configuring the receivers' beam patterns and the experimental geometry in order to achieve the maximum signal-to-noise ratios, so that the range of usable data was limited. While the experiment was designed with highly accurate timing instrumentation necessary to yield the precision to resolve the acoustic phase changes, there were no comparably accurate measurements made for positional reference points of the source and tow-body. This additional information would have made calibration of the tow-body track more accurate than the method used in Section IV. Further, no attempt was made at simulating autofocussing or other such filtering which may sometimes improve performance under these sorts of adverse conditions. These difficulties could be overcome in appropriate follow-on experiments.

In addition to the results reported here, it was originally hoped that the effect of internal waves, which can cause large changes in acoustic signal phase, would be evident in this data. However, in order to observe such phase changes, the synthetic aperture of an SAS system would have to transit the boundary of such a wave. To increase the occurrence of such an event, the dimensions of the synthetic aperture should be comparable to the dimensions of an internal wave. However, the experimental tracks were considerably smaller than such dimensions making the detection of an internal wave event very small.

Acknowledgments

References:

1. Underwater Acoustic System Analysis, Burdic, William S., Prentice-Hall, Inc., Englewood Cliffs, New Jersey, 076322, 1984, p. 127.

2. Statistical Antenna Theory, Shifrin, Yakov Solomonovich, The Golden Press, Boulder, Colorado, 1971.

Appendix A

Acoustic Data Runs

The purpose of this appendix is to condense the acoustic data from this experiment in such a fashion as to give the reader a very quick and qualitative understanding of the quality and amount of data collected. Each of the following pages contains six plots per page. For all plots, the abscissa is the ping number during a run. If the axis is labeled, "Amp" , the ordinate represents the maximum acoustic amplitude for each ping (time series). If the axis is labeled "Samp" the ordinate is the number of samples after the start of the received data record when the maximum amplitude occurs. The top 2 plots on each page represent the entire data set (all pings for a given run and a specified channel). The next 4 plots represent blow-ups of specific times (pings) along the track, usually for 2 different sections of the track corresponding to the pings closest to each transmitter.

Run 1: Channel 1
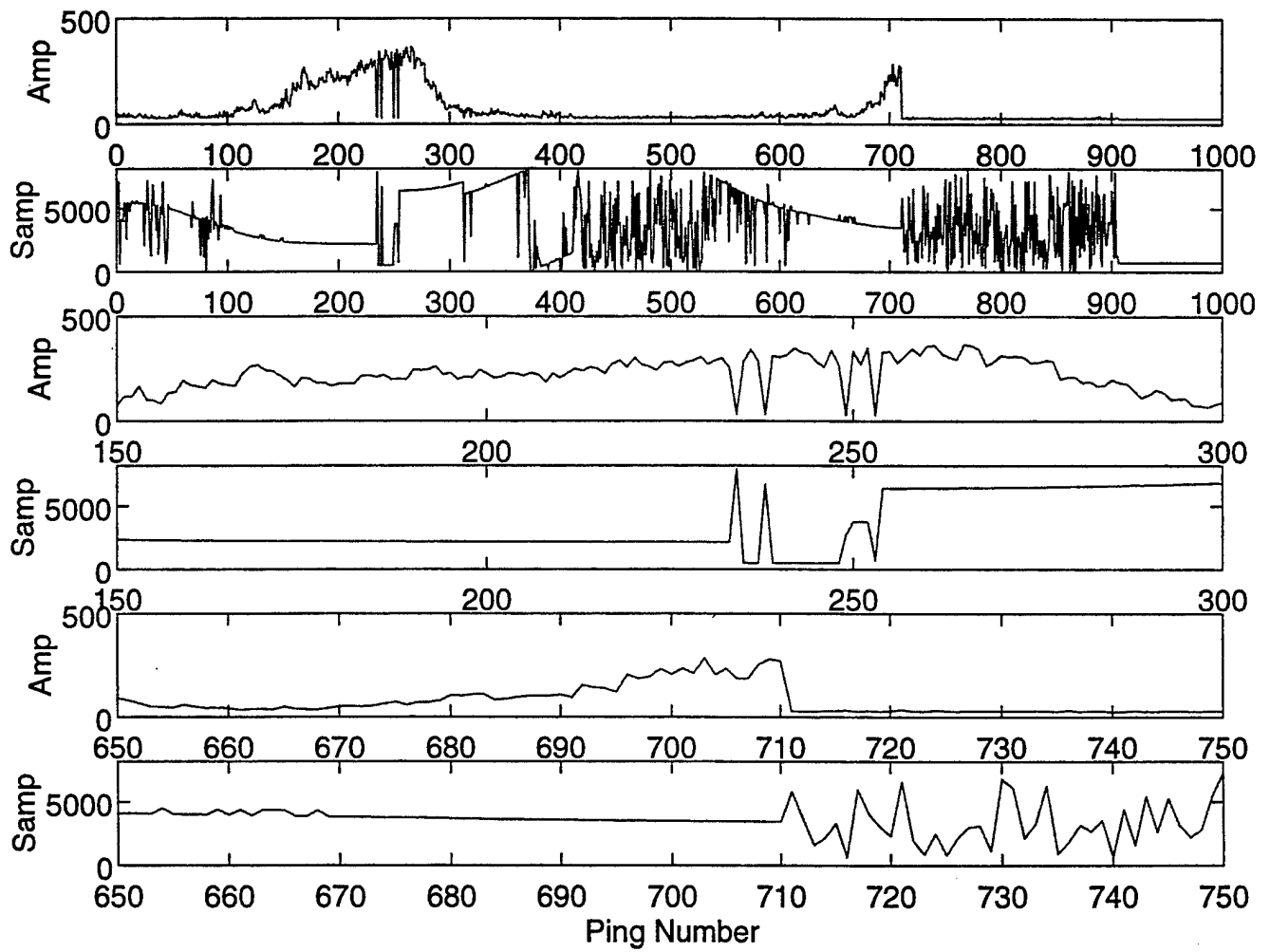
Run 1: Channel 2
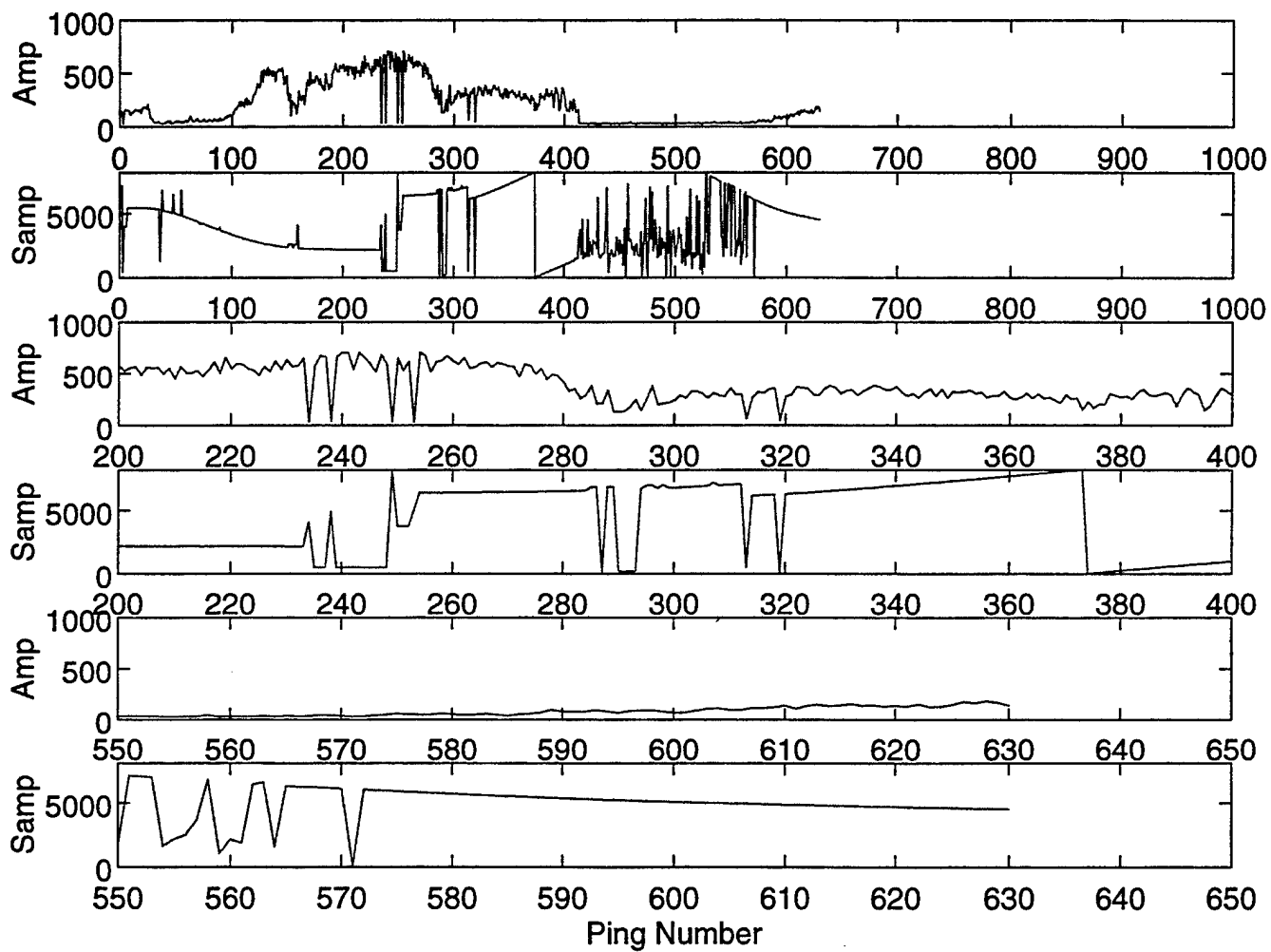
Run 2: Channel 1
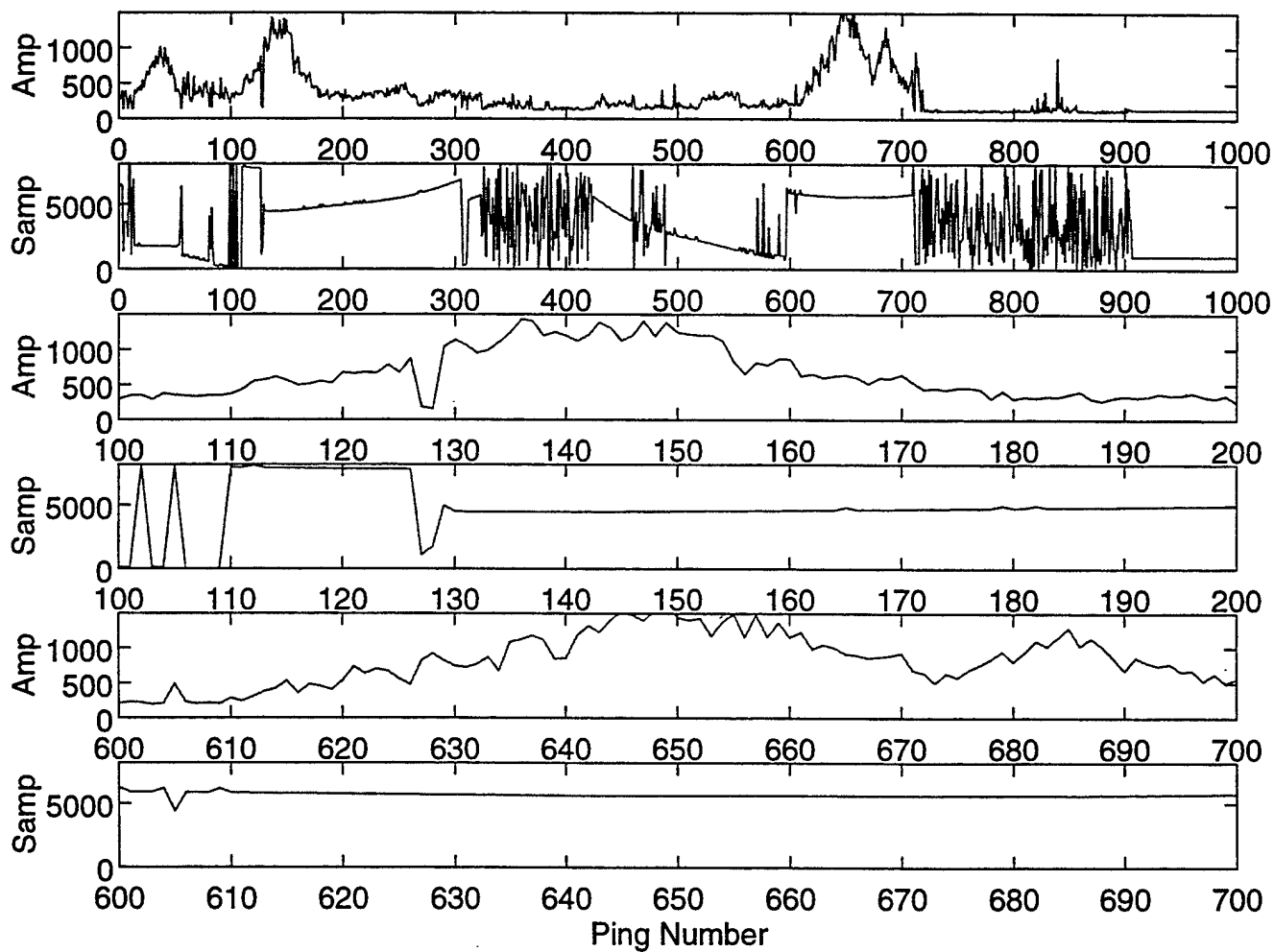
Run 2: Channel 2
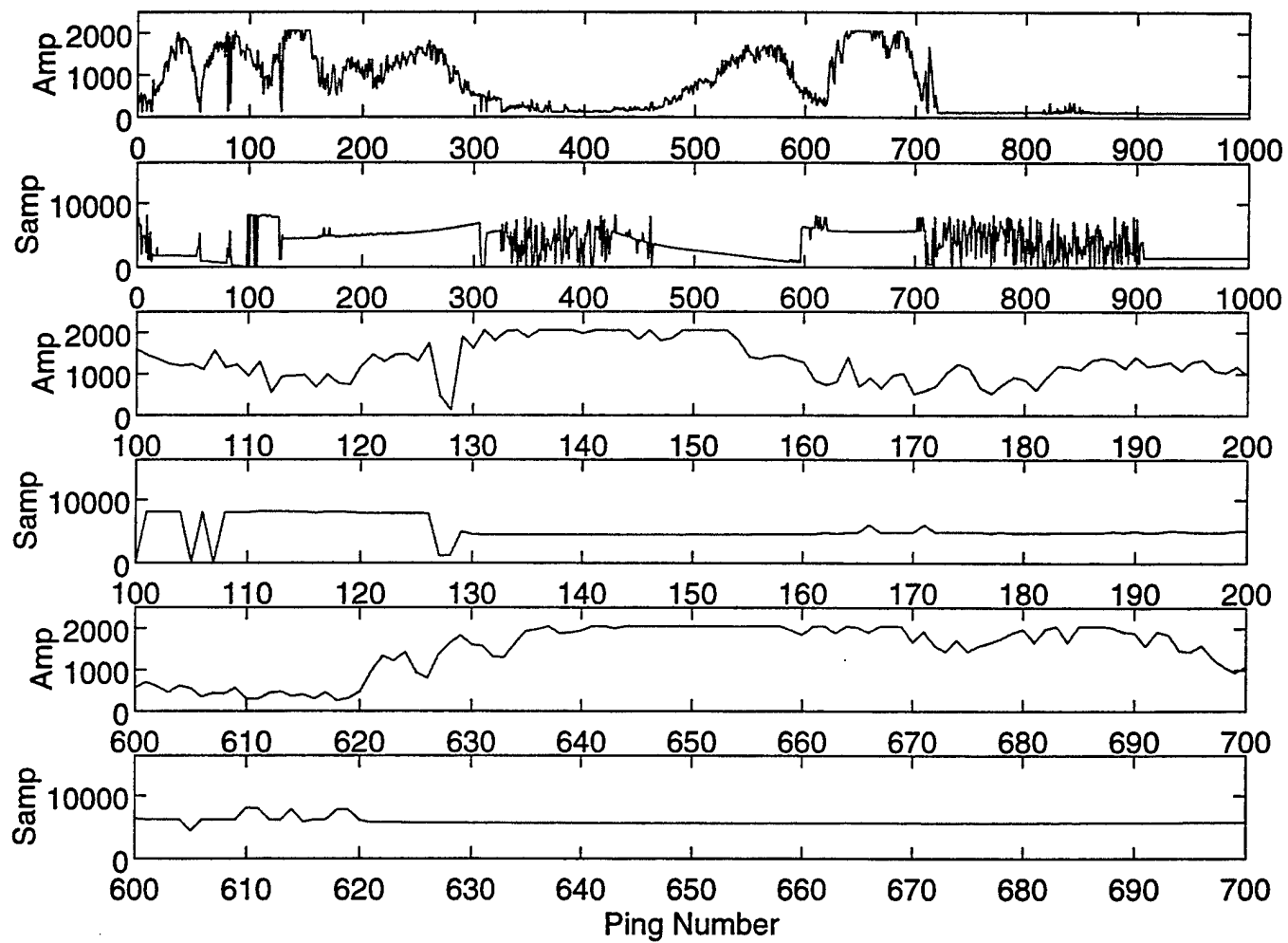
Run 3: Channel 1
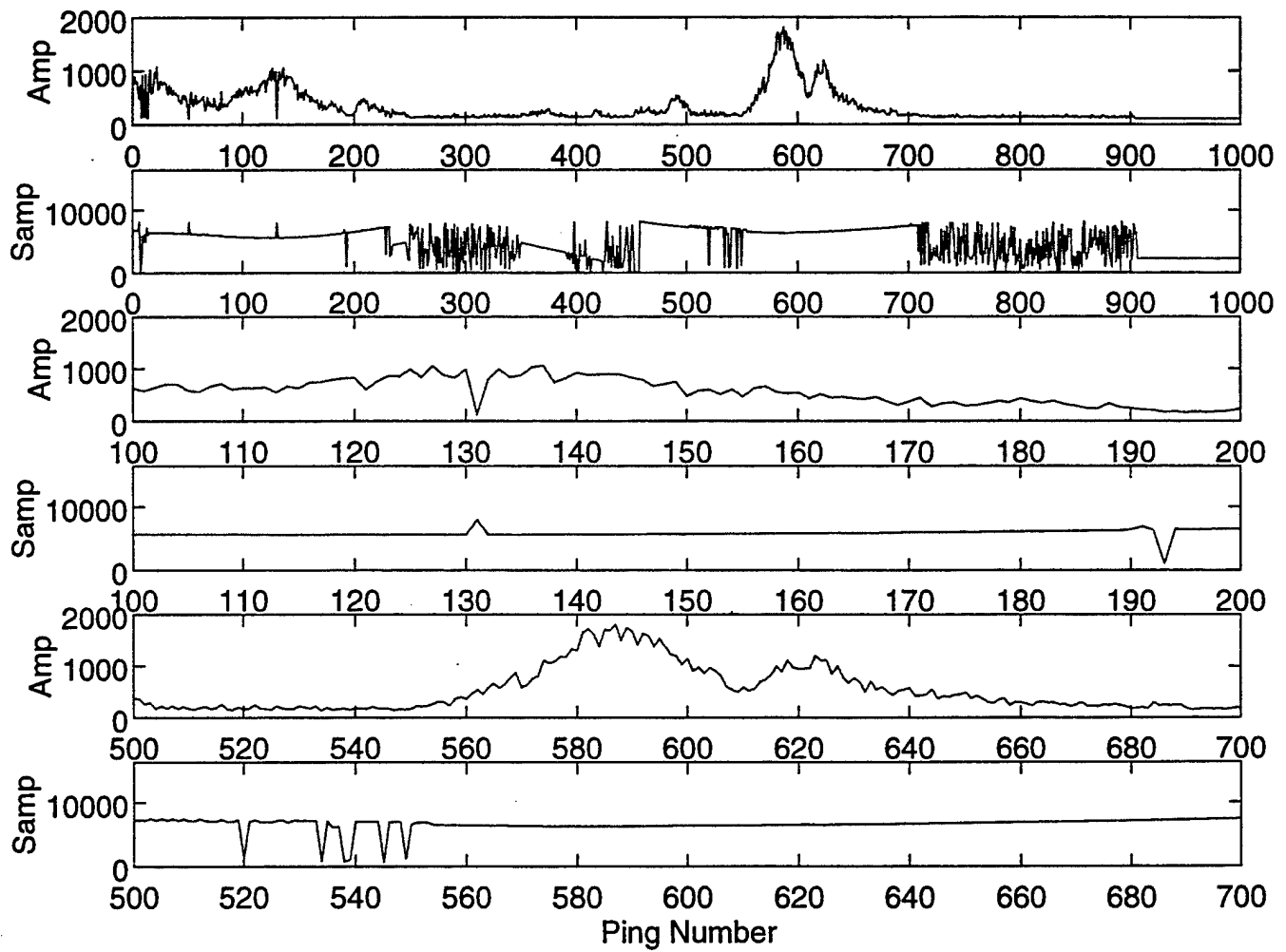
Run 3: Channel 2
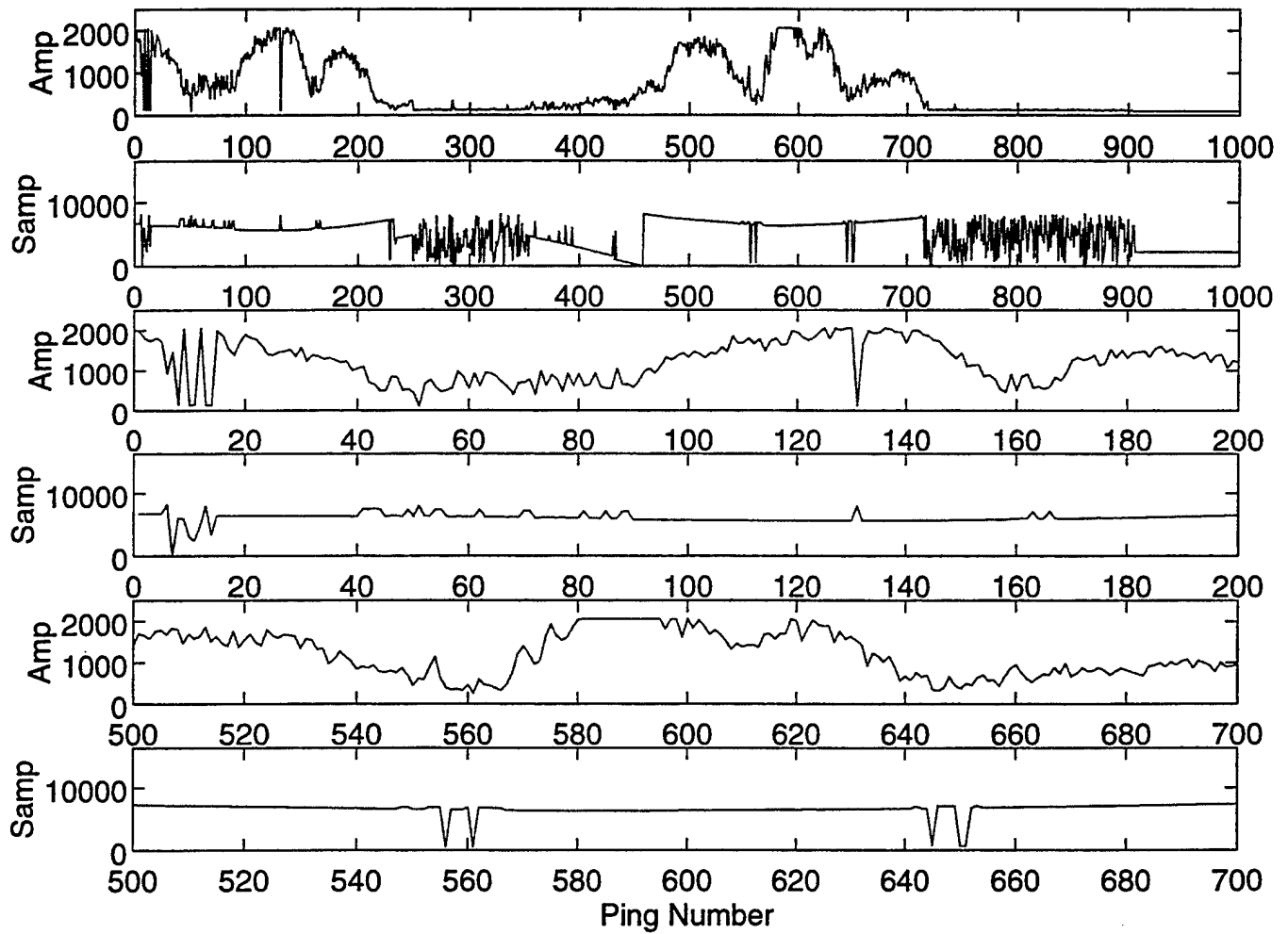
Run 6: Channel 2
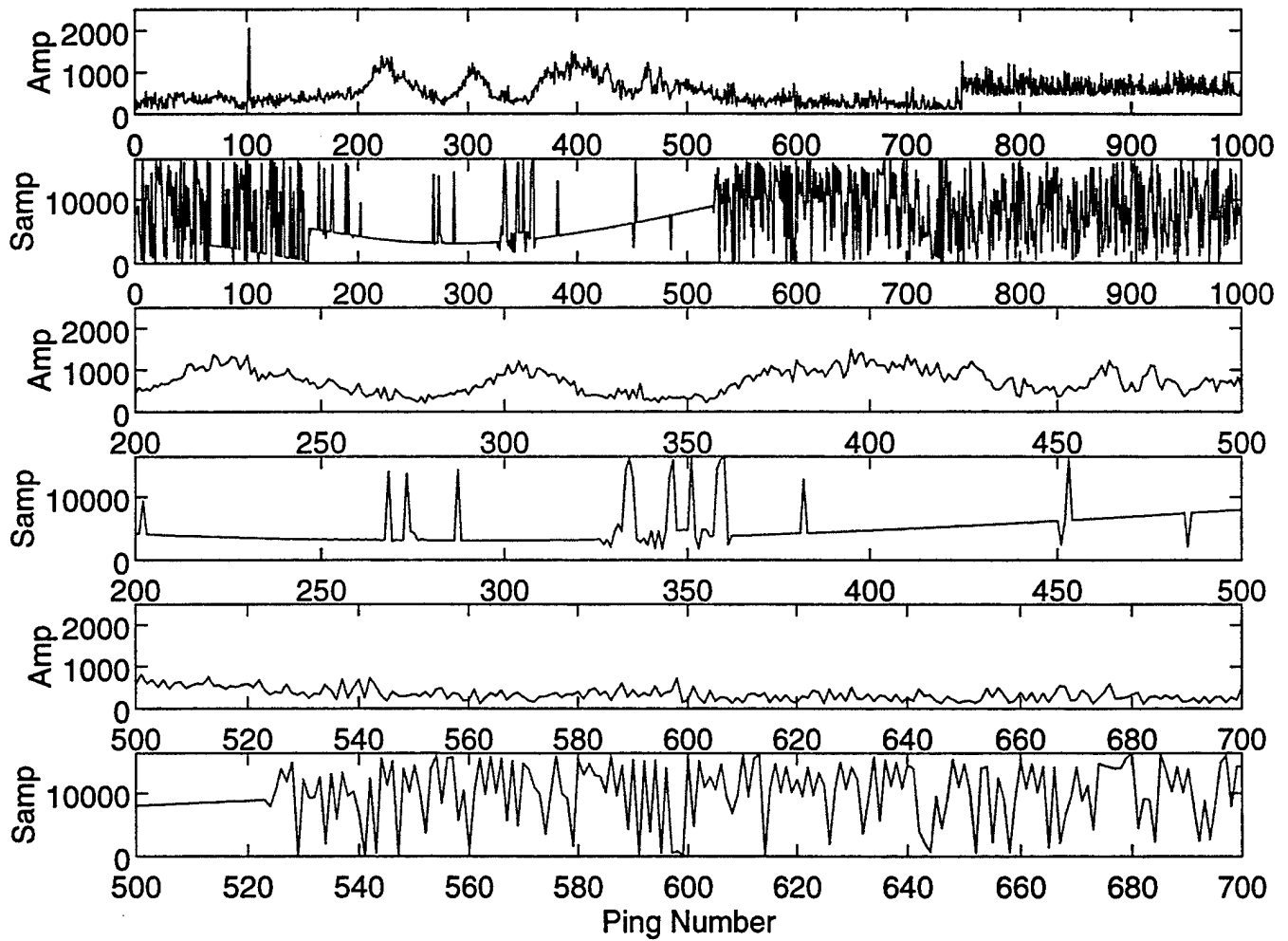
Run 7: Channel 1
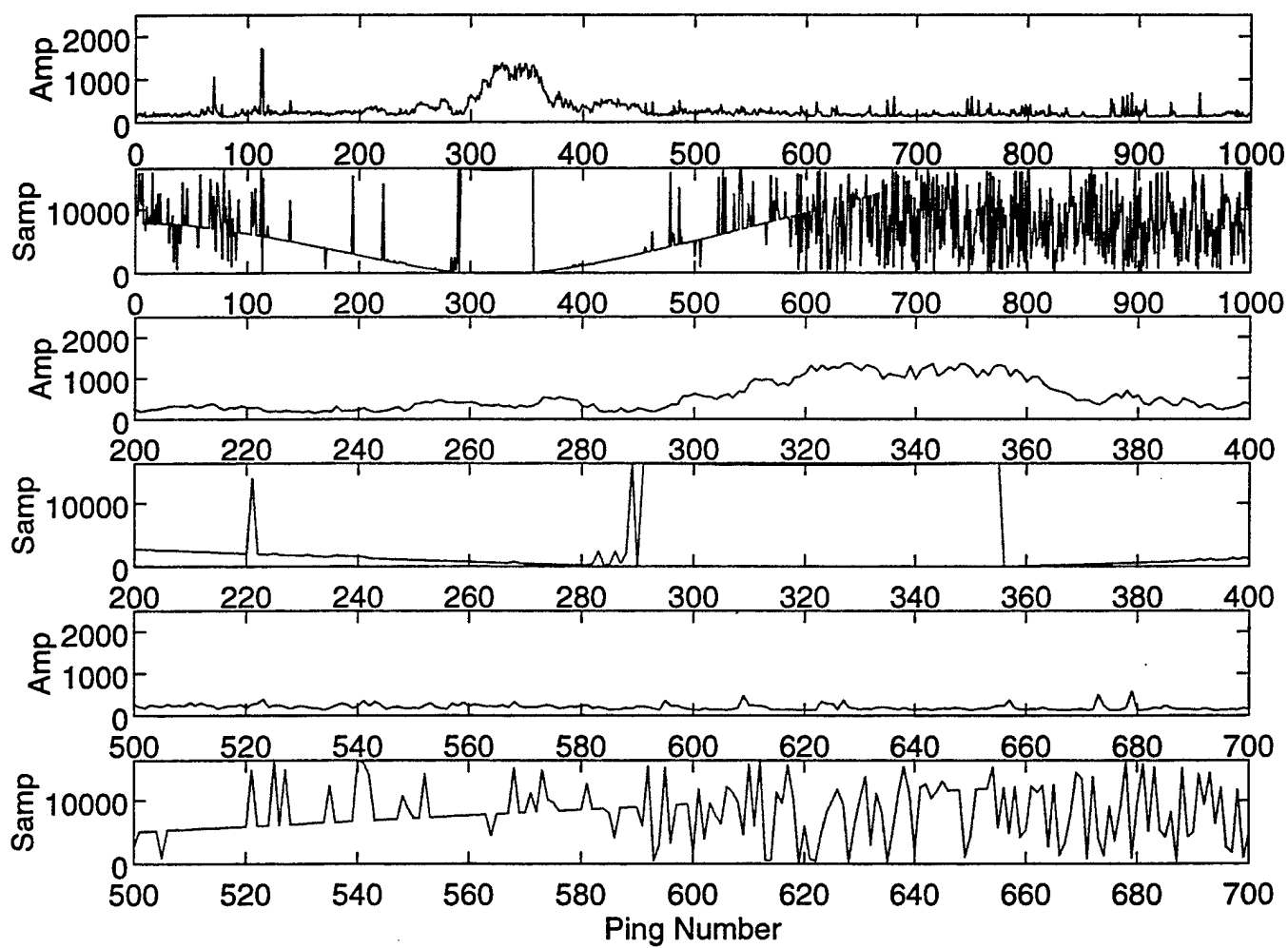
Run 7: Channel 2
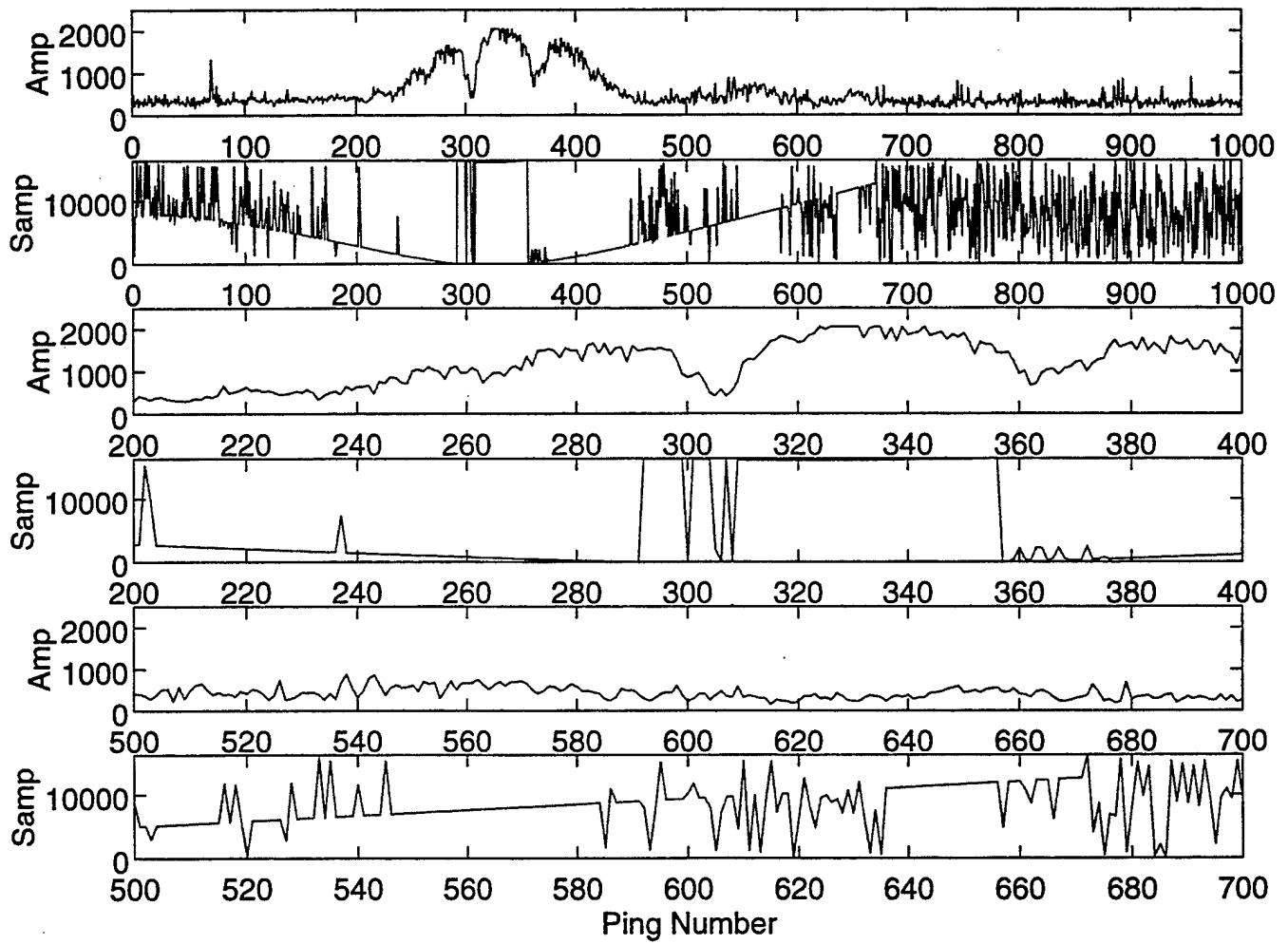
Run 8: Channel 1

Run 8: Channel 2

Ping Number
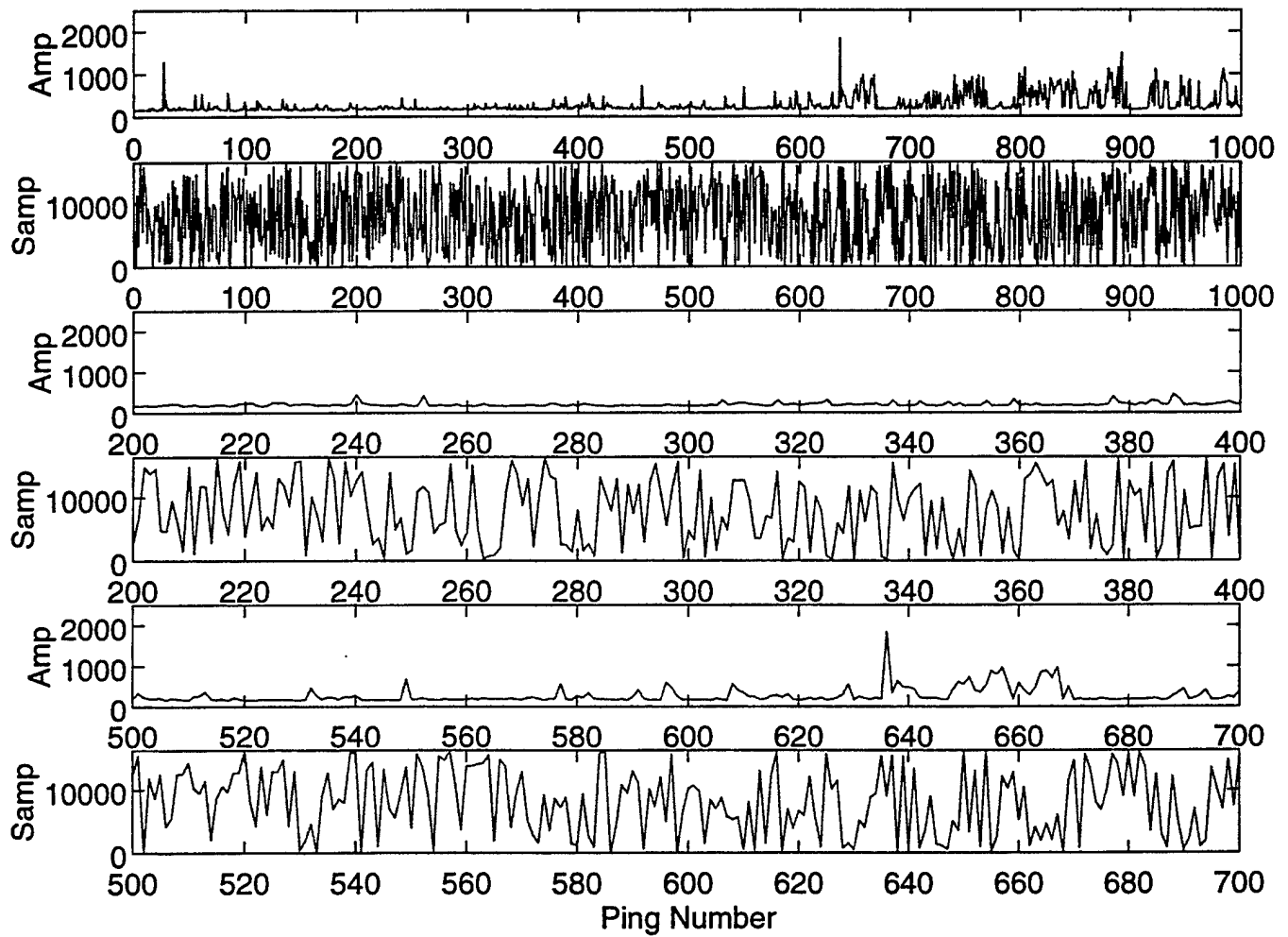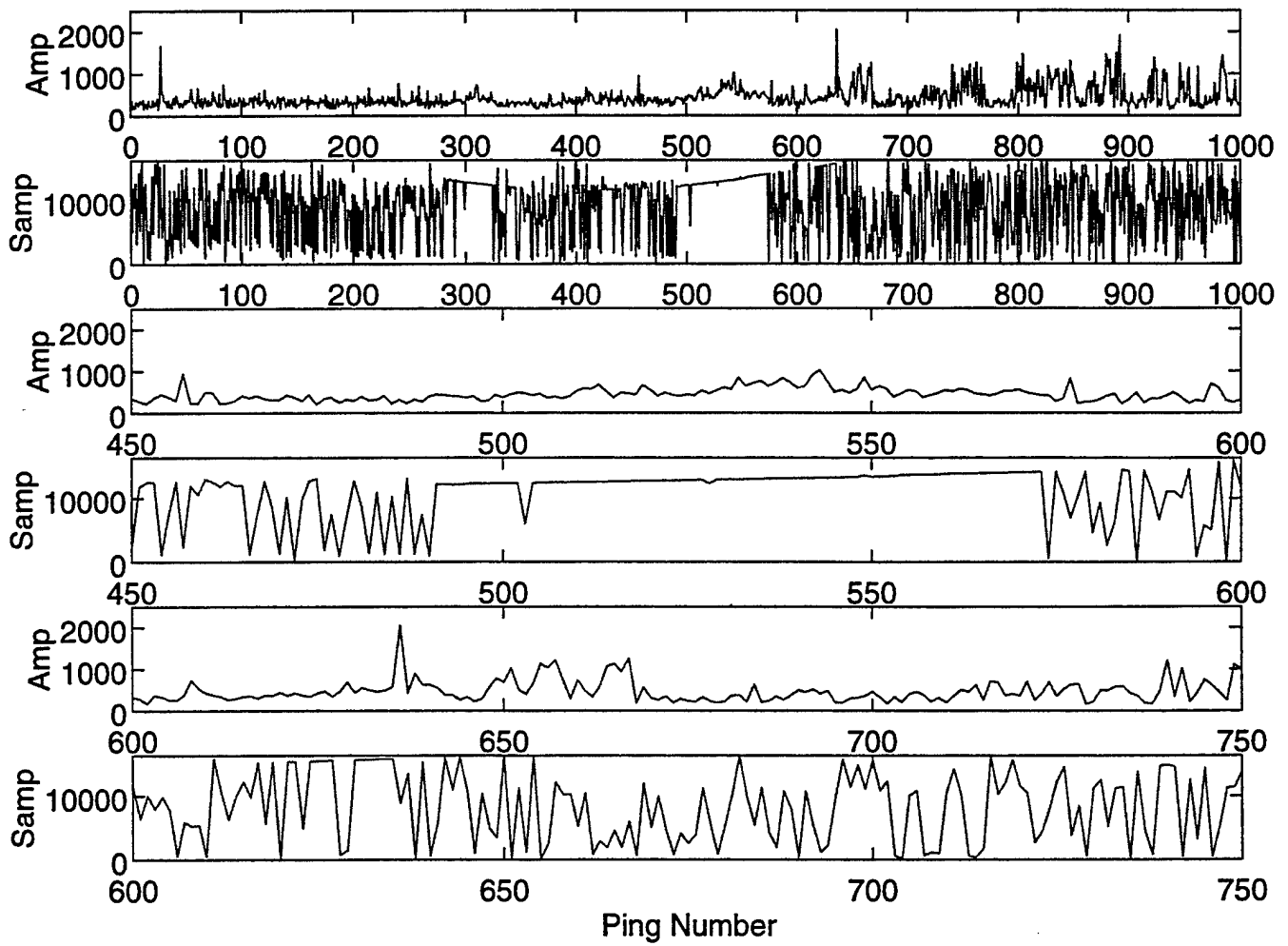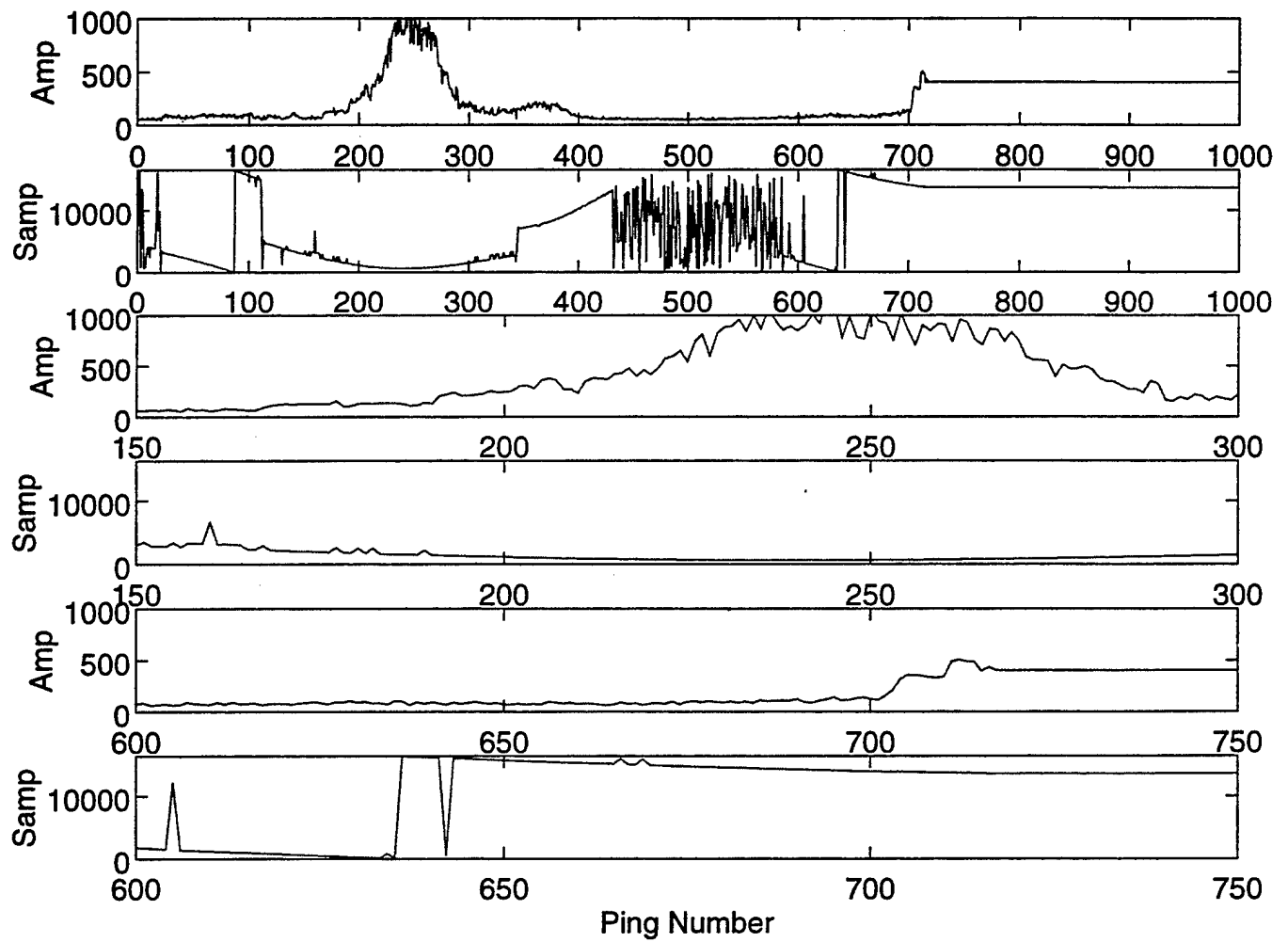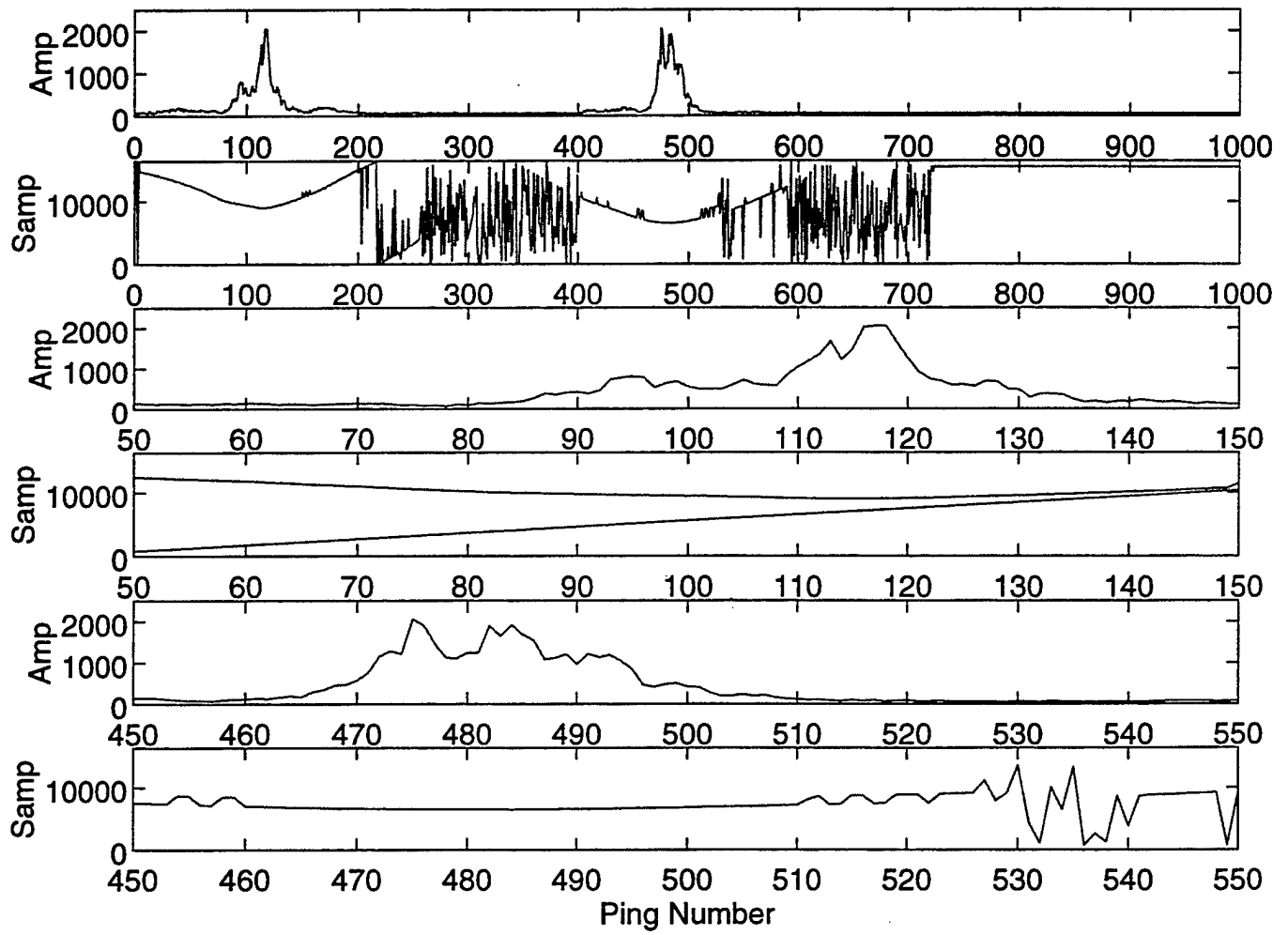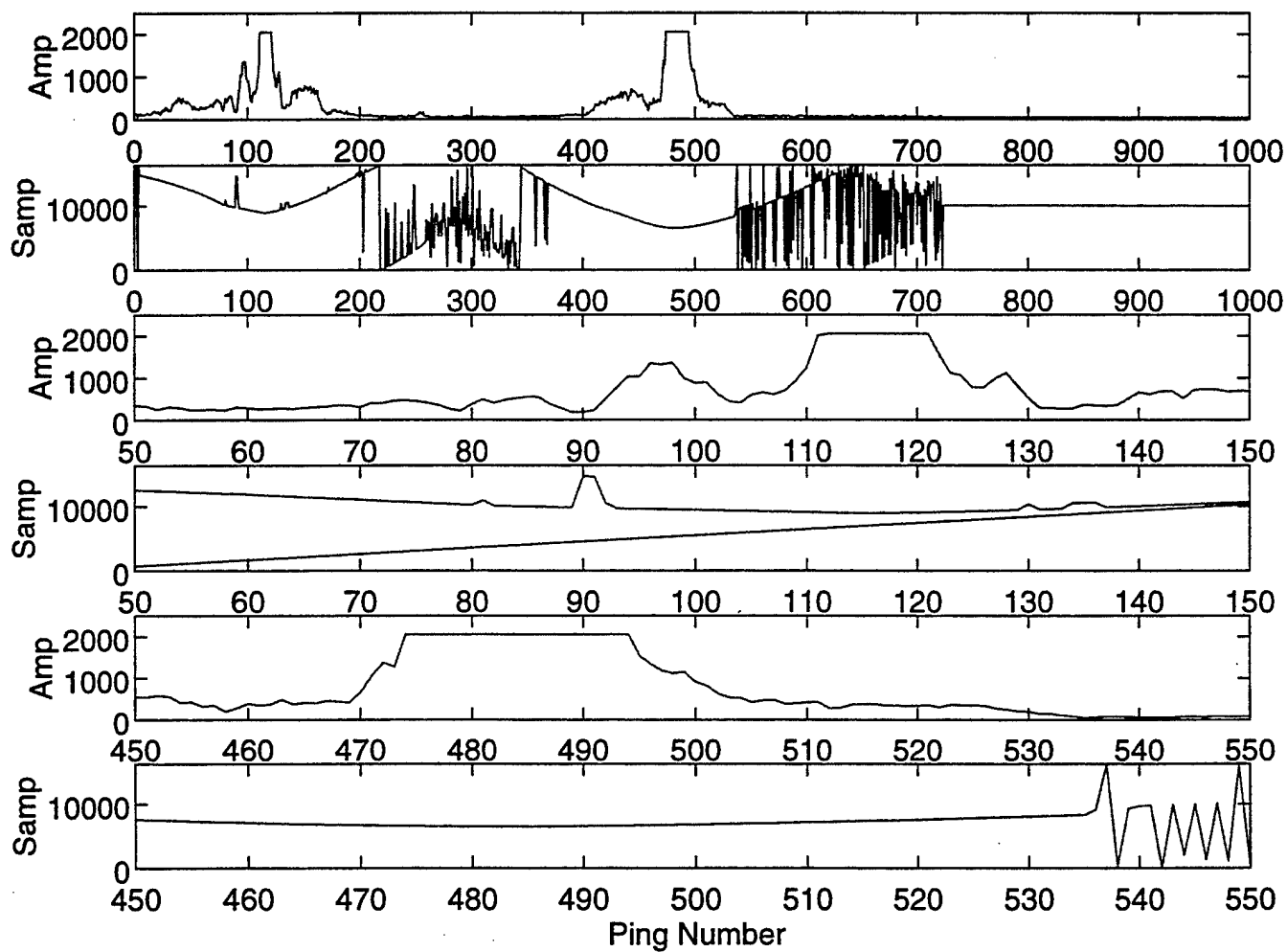
Run 10: Channel 1

Run 10: Channel 2
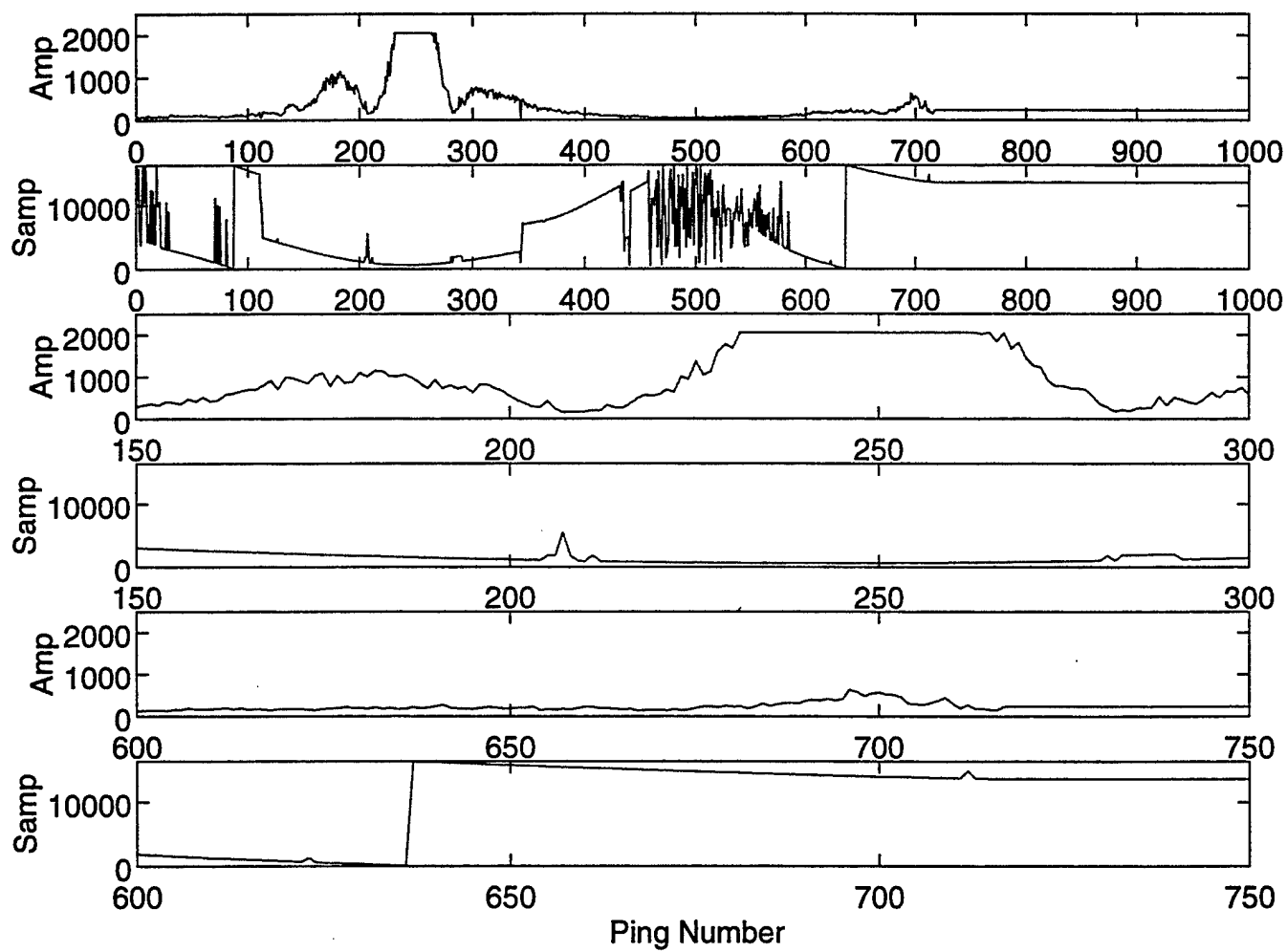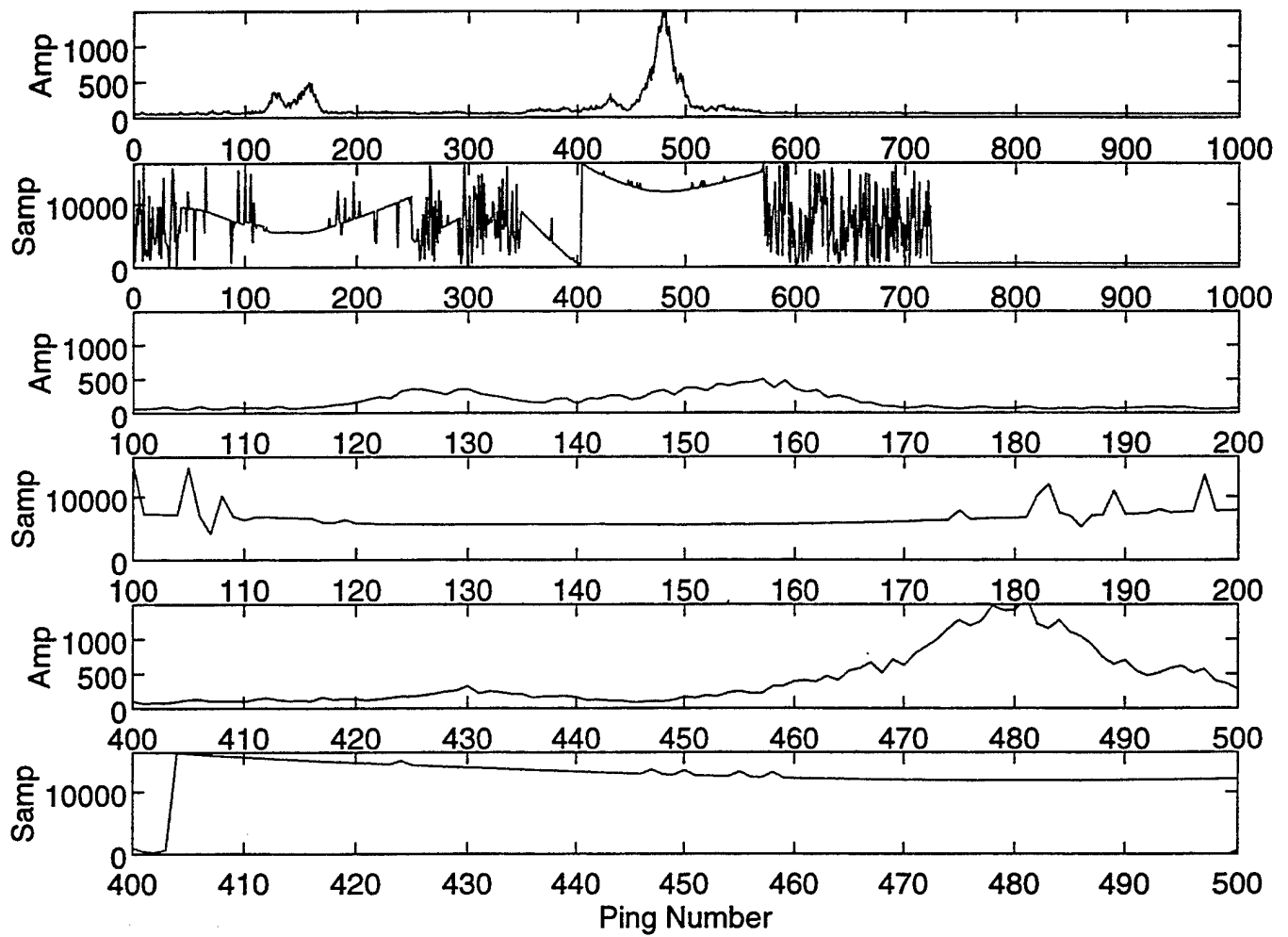
Run 11: Channel 1
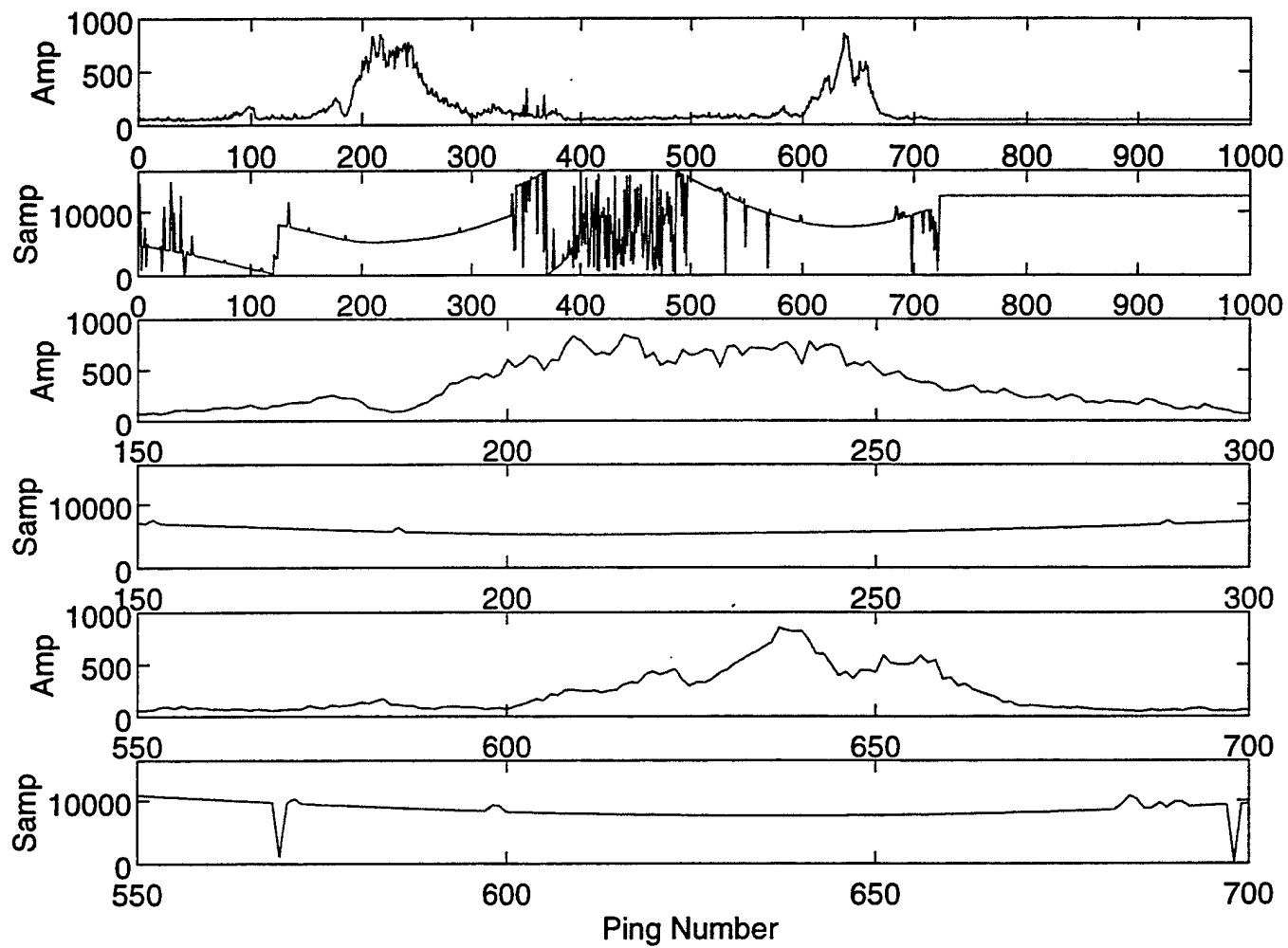
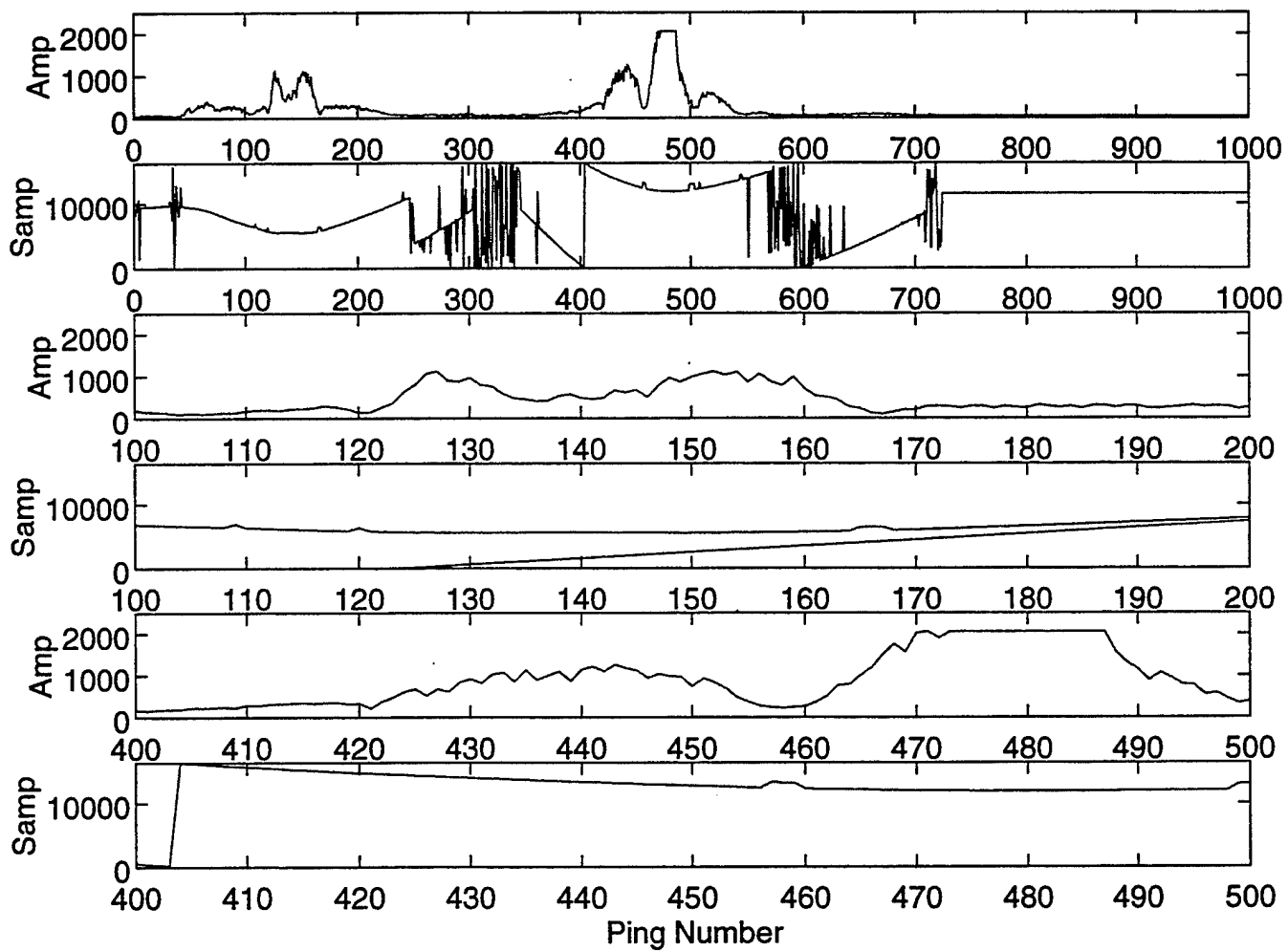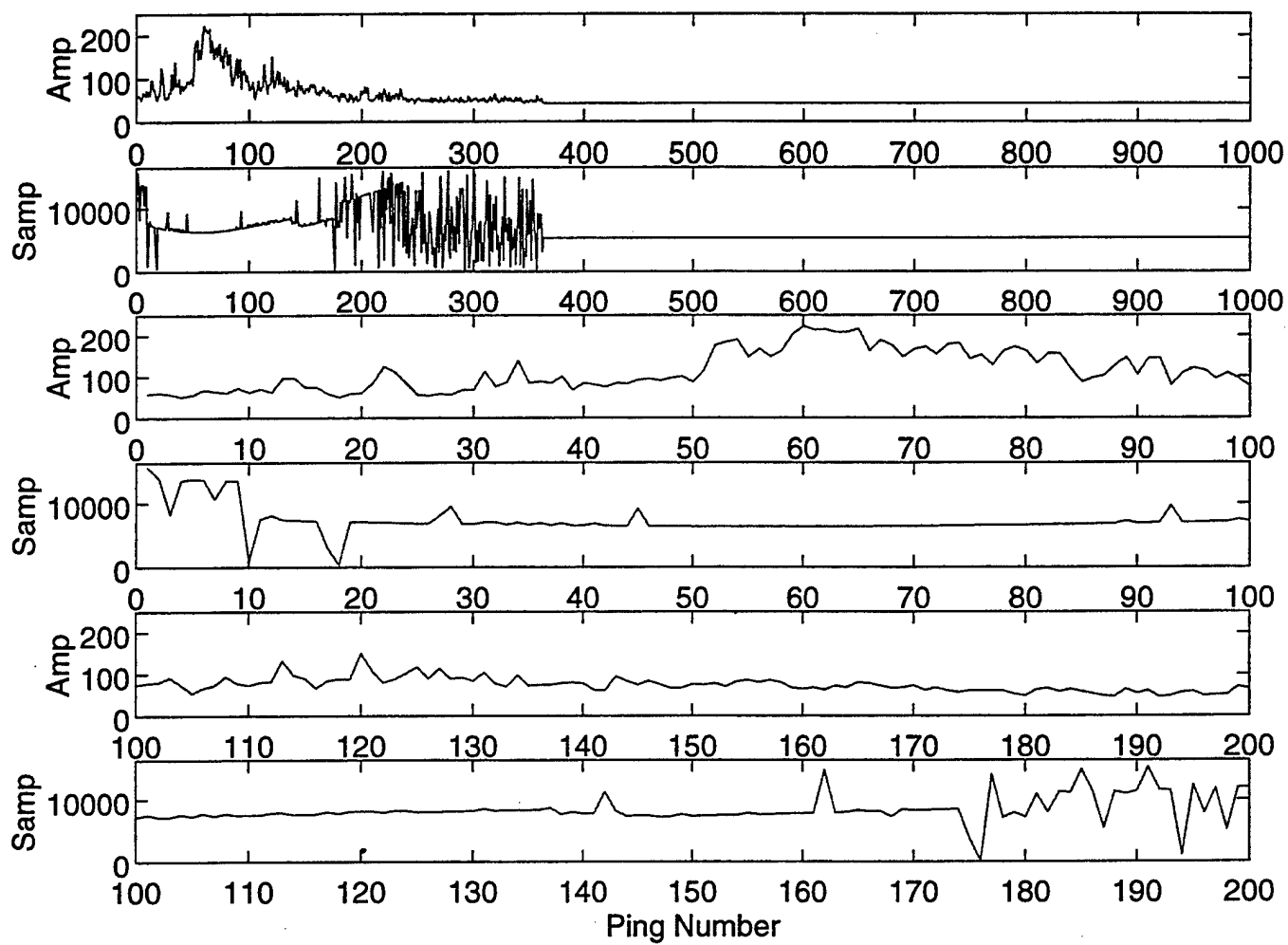Run 11: Channel 2
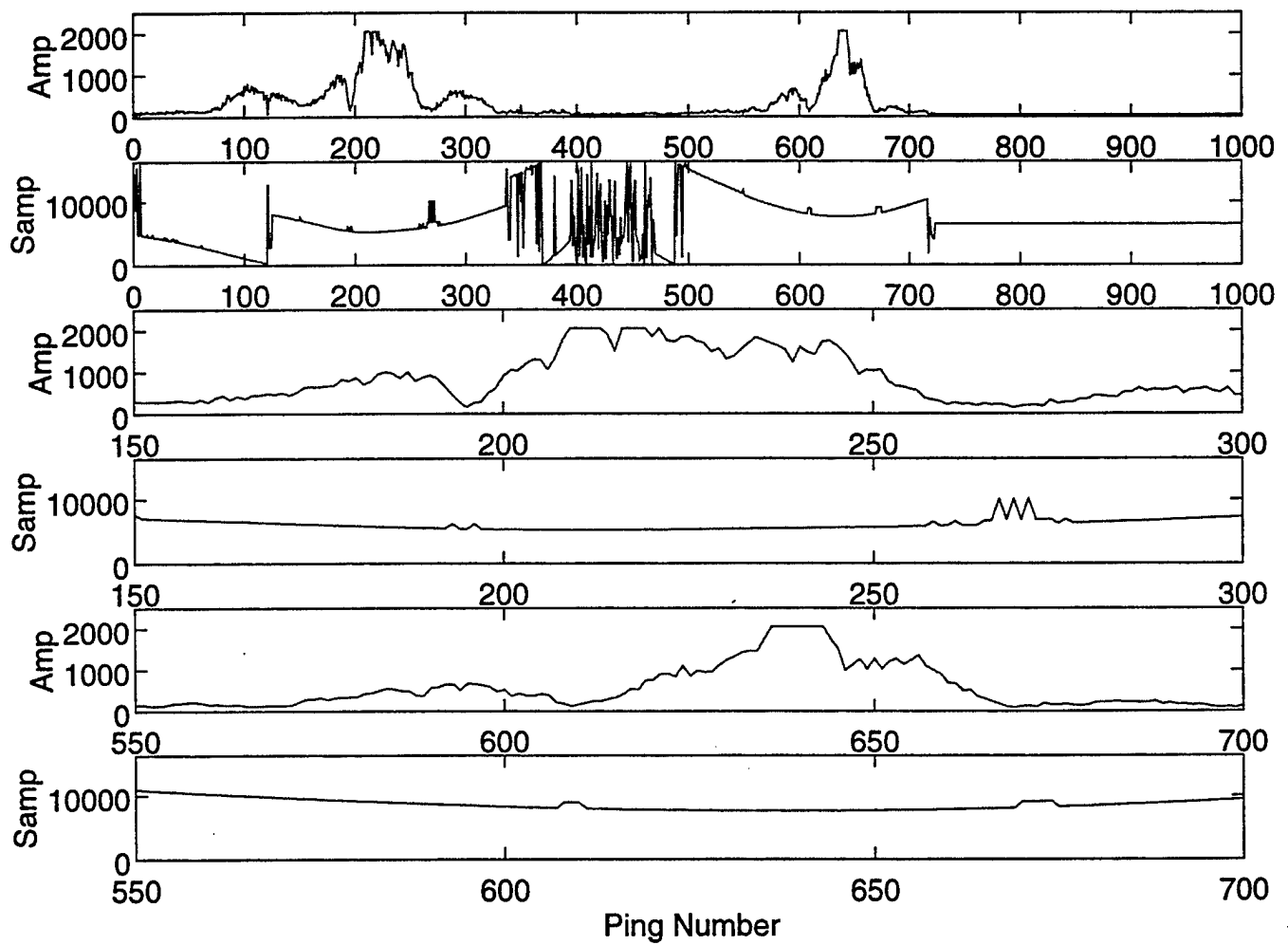
Run 13: Channel 1
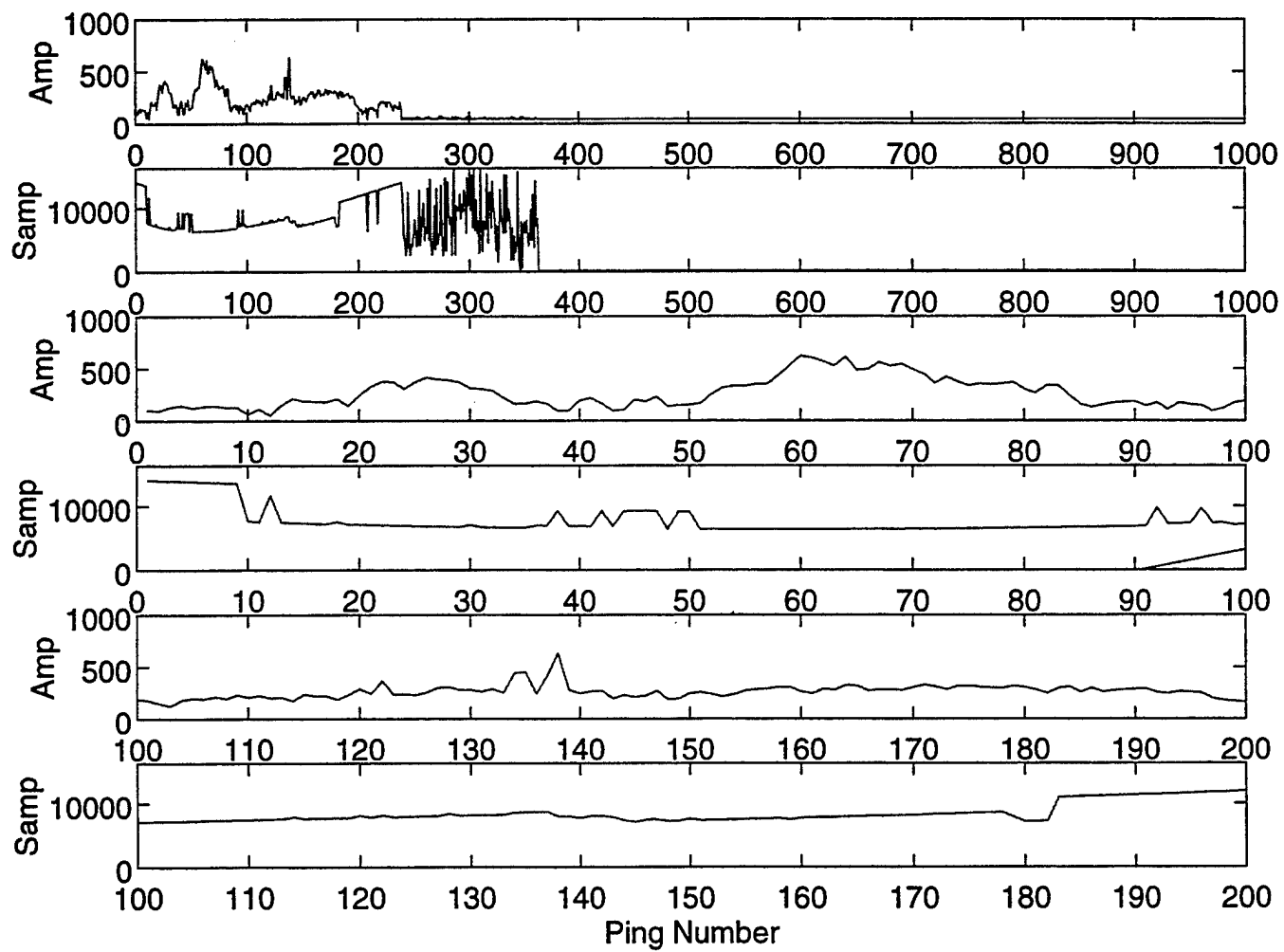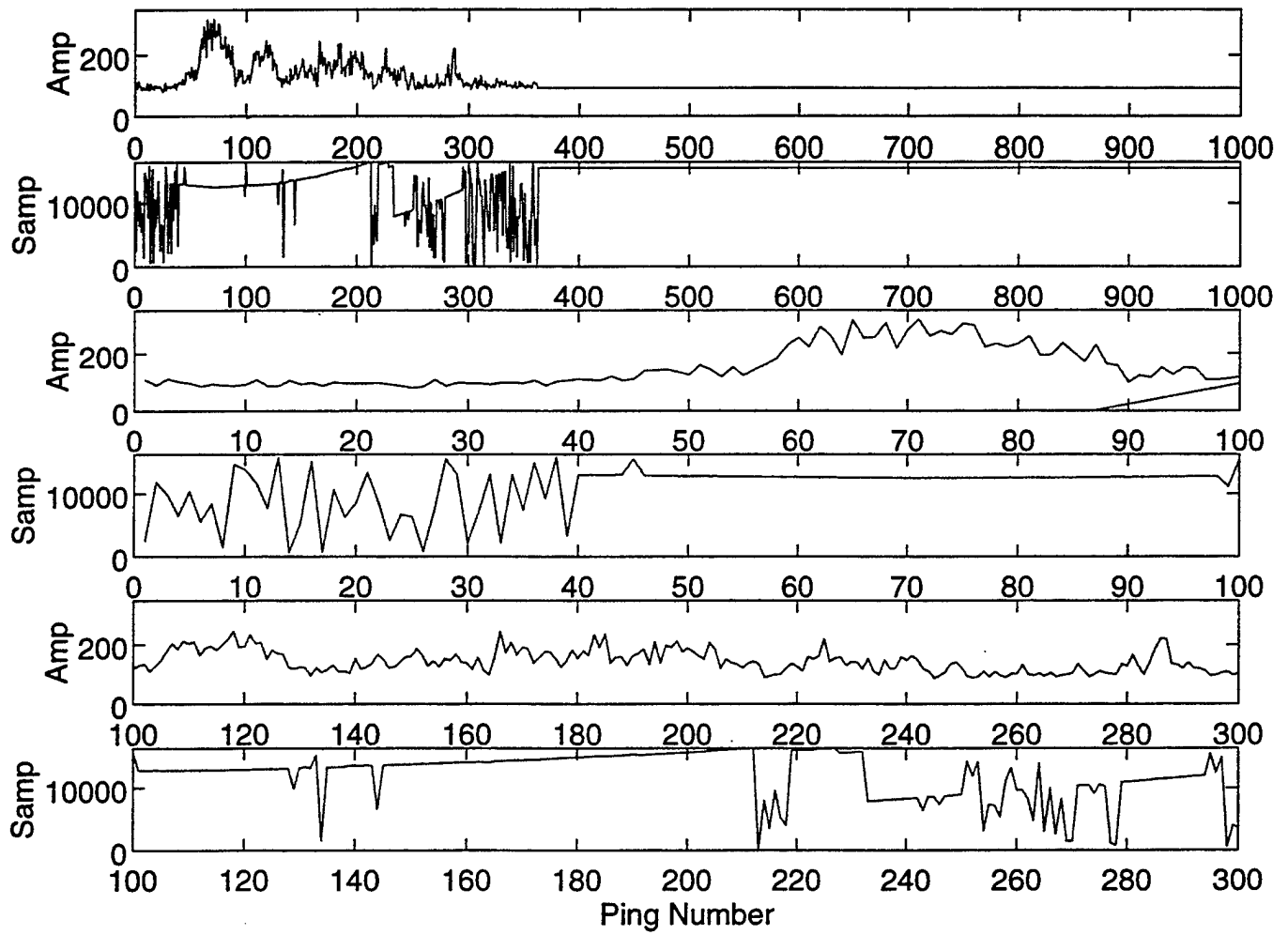
Run 13: Channel 2

Run 14: Channel 1

Run 14: Channel 2
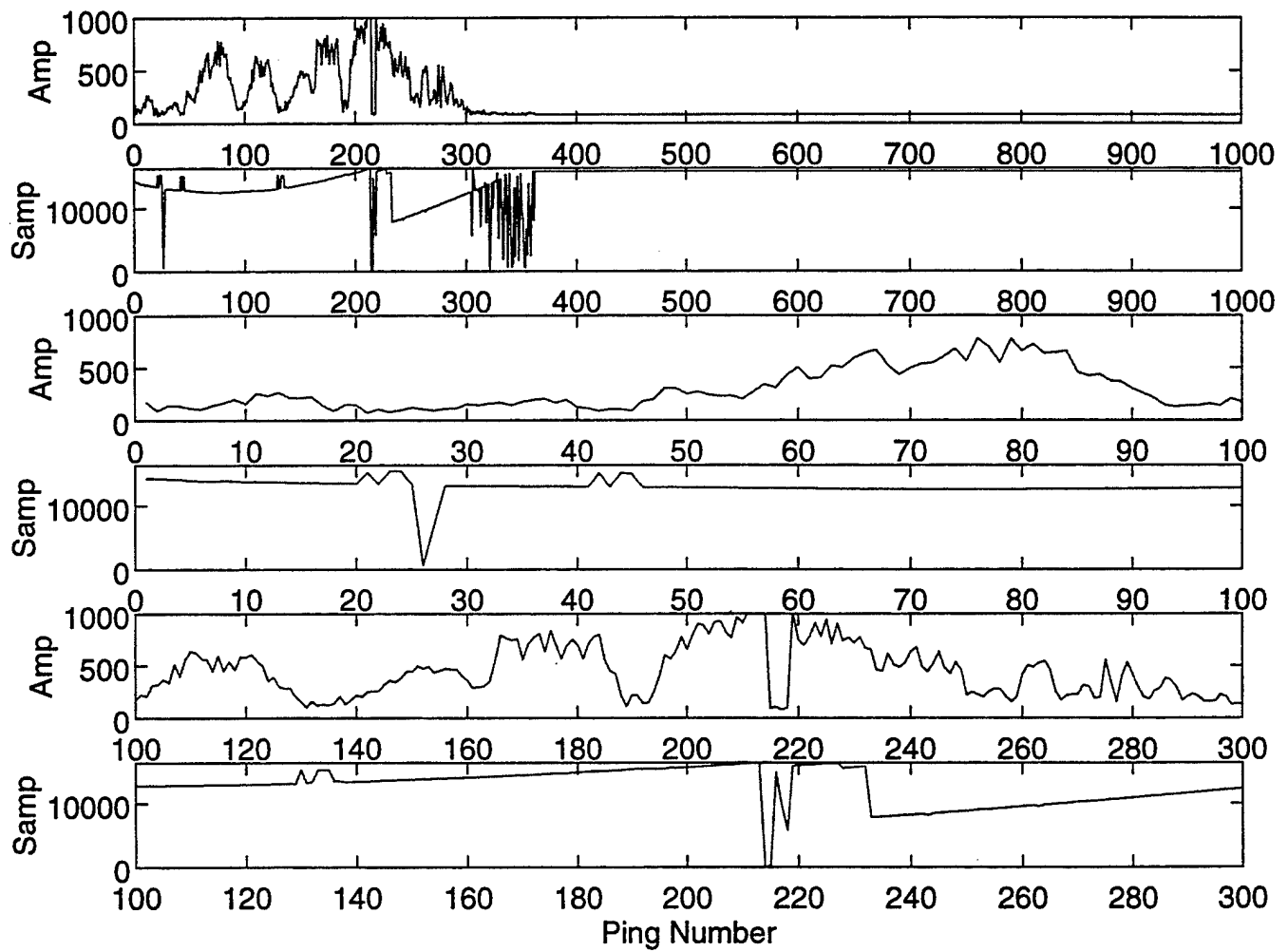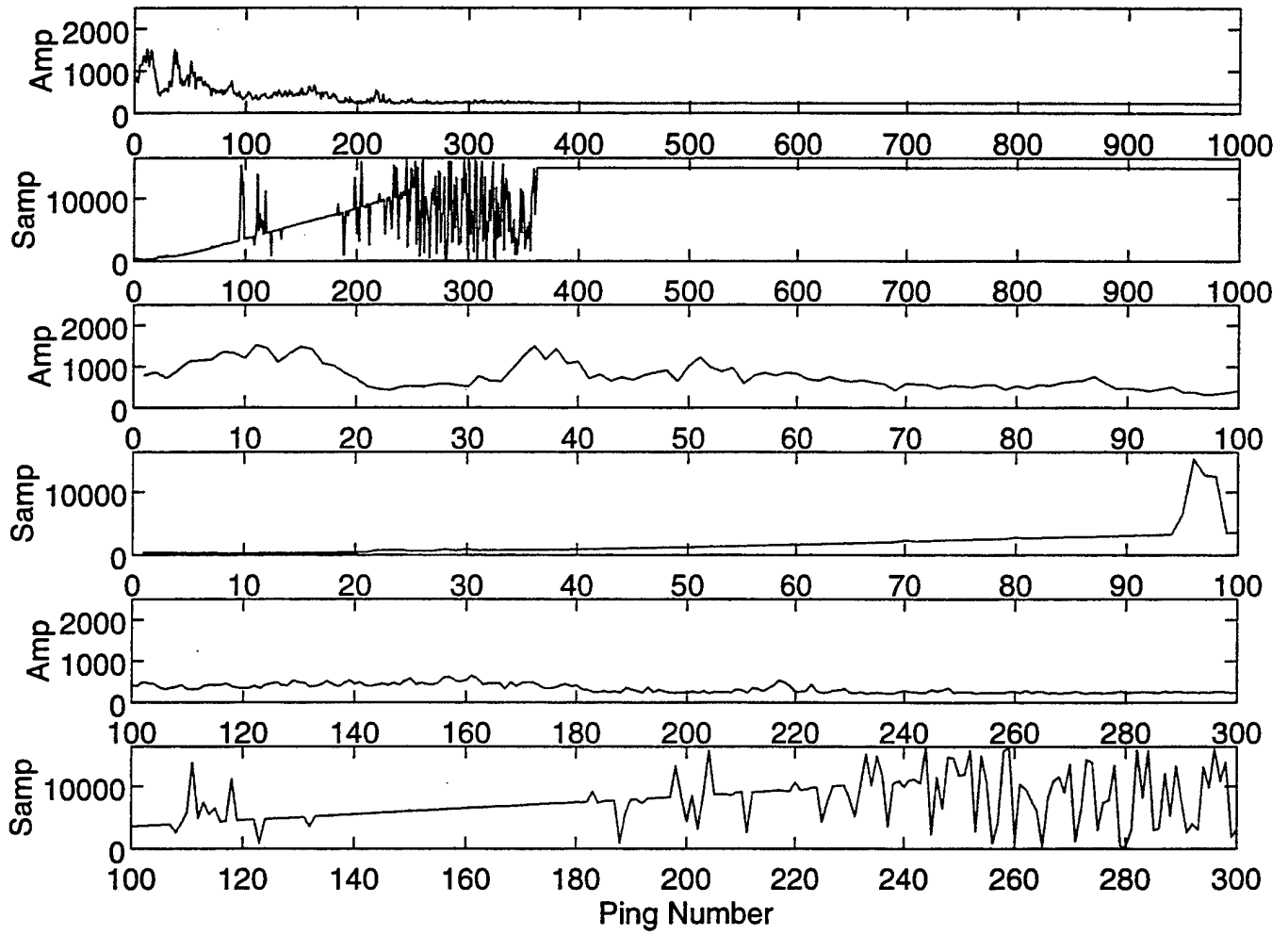
Run 15: Channel 1

Run 15: Channel 2

Run 16: Channel 1

Run 16: Channel 2

Run 17: Channel 1

Run 17: Channel 2